Title

Sensitivities of the West Greenland Current to Greenland Ice Sheet Meltwater in a Mesoscale Ocean/Sea Ice Model

Journal

Journal of Physical Oceanography, 54(7)

ISSN

0022-3670

Authors

Morrison, Theresa J

McClean, Julie L

Gille, Sarah T

et al.

Publication Date

2024-07-01

DOI

10.1175/jpo-d-23-0102.1

Sensitivities of the West Greenland Current to Greenland Ice Sheet Meltwater in a Mesoscale Ocean/Sea Ice Model

THERESA J. MORRISON,[a,b] JULIE L. MCCLEAN,[a] SARAH T. GILLE,[a] MATHEW E. MALTRUD,[c] DETELINA P. IVANOVA,[d] AND ANTHONY P. CRAIG[e]

[a] *Scripps Institution of Oceanography, La Jolla, California*
[b] *Princeton University, Princeton, New Jersey*
[c] *Los Alamos National Laboratory, Los Alamos, New Mexico*
[d] *Climformatics, Fremont, California*
[e] *Anthony Craig LLC, Seattle, Washington*

(Manuscript received 7 June 2023, in final form 15 March 2024, accepted 23 March 2024)

ABSTRACT: Meltwater from the Greenland Ice Sheet can alter the continental shelf/slope circulation and cross-shelf freshwater fluxes and limit deep convection in adjacent basins through surface freshening. We explore the impacts on the West Greenland Current and eastern Labrador Sea with different vertical distributions of the meltwater forcing. In this study, we present the results from global coupled ocean/sea ice simulations, forced with atmospheric reanalysis, that are mesoscale eddy-active (~2–3-km horizontal spacing) and eddy-permitting (~6–7-km horizontal spacing) in the study region. We compare the West Greenland Current in mesoscale eddy-active and eddy-permitting without meltwater to highlight the role of small-scale features. The mesoscale eddy-active configuration is then used to assess the change in the eastern Labrador Sea when meltwater is added to the surface or vertically distributed to account for mixing within fjords. In both simulations with meltwater, the West Greenland and West Greenland Coastal Currents are faster than in the simulation with no meltwater; their mean surface speeds are the highest in the vertical distribution case. In the latter case, there is enhanced baroclinic conversion at the shelf break compared to the simulation with no meltwater. When meltwater is vertically distributed, there is an increase in baroclinic conversion at the shelf break associated with increased eddy kinetic energy. In addition, in the eastern Labrador Sea, the salinity is lower and the meltwater volume is greater when meltwater is vertically distributed. Therefore, the West Greenland Current is sensitive to how meltwater is added to the ocean with implications for the freshening of the Labrador Sea.

SIGNIFICANCE STATEMENT: Our goal is to understand how the flux of freshwater across the West Greenland continental slope into the Labrador Sea is modified by meltwater from the Greenland Ice Sheet. We compare the simulations of the ocean that capture key dynamics along the West Greenland continental slope that have no meltwater, meltwater added to the ocean surface, and meltwater distributed vertically to represent the mixing within fjords. When meltwater is added, the currents along the continental slope are faster, with the greatest increase when meltwater is vertically distributed. In that case, there is enhanced freshening of the Labrador Sea because modified density gradients generate more eddies. Proper representation of the vertical structure of meltwater is important for projecting the impact of freshwater on the subpolar North Atlantic.

KEYWORDS: Continental shelf/slope; North Atlantic Ocean; Mesoscale processes; Mesoscale models; Ocean models

1. Introduction

Projections of the future climate under anthropogenic forcing have indicated the potential for a decline in the Atlantic meridional overturning circulation (AMOC) strength, in part, as a result of freshening of the subpolar North Atlantic; see Weijer et al. (2019) for a review of this topic. Freshening of the subpolar North Atlantic could be the result of a slowdown of the AMOC itself (a salt-advection feedback), increased freshwater export from the Arctic Ocean, or mass loss from the Greenland Ice Sheet (GIS). The possibility of GIS meltwater reducing deep convection and subsequently weakening the AMOC depends on meltwater crossing the continental shelf break and entering the deep basin where deep water formation occurs.

Deep water formation has been observed in the Labrador Sea, Irminger Sea, and Nordic seas (Petit et al. 2020; Chafik and Rossby 2019; Desbruyères et al. 2019). The results of the Overturning in the Subpolar North Atlantic Program (O-SNAP) (Lozier et al. 2019; Desbruyères et al. 2019) and other recent observations (Chafik and Rossby 2019) have furthered a shift away from the paradigm of deep convection and North Atlantic Deep Water (NADW) formation occurring primarily in the Labrador Sea. These observations cover a relatively short period considering the long time scales associated with AMOC variability and stand in contrast to ocean modeling studies showing that deep convection in the Labrador Sea contributes to AMOC variability (Yeager et al. 2021).

Supplemental information related to this paper is available at the Journals Online website: https://doi.org/10.1175/JPO-D-23-0102.s1.

Corresponding author: Theresa J. Morrison, t4morris@ucsd.edu

DOI: 10.1175/JPO-D-23-0102.1

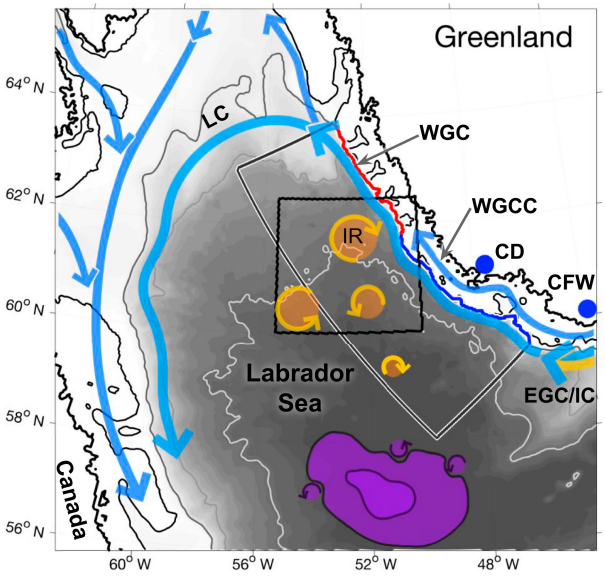

FIG. 1. Schematic of circulation in the Labrador Sea; isobaths are plotted at 400, 800, and 3000 m. Major currents are labeled: EGC/IC, WGC, WGCC, and Labrador Current (LC). The deep convection region is shown in purple. CFW and CD are indicated by blue dots. The high eddy kinetic energy region is indicated by the black rectangle (defined as 60°–62.5°N and 50°–55.5°W). Irminger Rings (IR; yellow) are shown in this area. The west Greenland shelf break is shown in dark blue (southern shelf break) and red (northern shelf break). The boundary of the eastern Labrador Sea control volume is shown in gray. Schematic is after Holliday et al. (2018) with additions from Sutherland and Pickart (2008), Håvik et al. (2017), Rossby et al. (2018), Rieck et al. (2019), Pacini et al. (2020).

The complex currents of the subpolar North Atlantic provide the source water from the subtropics to these deep water formation sites.

Warm, saline water from the subtropics is advected northward from the Gulf Stream in the North Atlantic Current (NAC). The eastern branches of the NAC extend into the Nordic seas, and the western branches form the Irminger Current (IC) (Holliday et al. 2018). The IC retroflects south of the Denmark Strait and flows south along the Greenland continental shelf break. The East Greenland Current (EGC) flows southward along the shelf break from Fram Strait to Cape Farewell (CFW in Fig. 1), transporting relatively cold freshwater and sea ice from the Arctic. The weaker and narrower East Greenland Coastal Current (EGCC) is present onshore of the EGC both north and south of the Denmark Strait (Håvik et al. 2017; Sutherland and Pickart 2008; Foukal et al. 2020). South of the Denmark Strait, the EGC is inshore of the IC; at Cape Farewell, the EGC and IC merge and turn northward to flow along the western Greenland shelf, forming the West Greenland Current (WGC). The EGCC remains farther onshore and becomes the West Greenland Coastal Current (Pacini et al. 2020). The WGC meanders and produces eddies near Cape Desolation (CD in Fig. 1) (Pacini and Pickart 2022). Irminger Rings are large (30–60 km) and long-lived (1–2 years) and are shed from the WGC near Cape Desolation where steep bathymetry produces instabilities (Eden and Böning 2002; Chanut et al. 2008). These eddies could have a restratifying effect on the Labrador Sea (Chanut et al. 2008), although it is possible that they do not travel far enough south to interact with the convective region (Rieck et al. 2019).

However, eddy advection has been shown to contribute to the transport of freshwater off the southwest Greenland continental shelf (Katsman et al. 2004; Bracco et al. 2008; de Jong et al. 2014). This transport has also been linked to Ekman transport (Luo et al. 2016; Schulze Chretien and Frajka-Williams 2018) in both modeling and observation-based studies. Late summer and early autumn have been identified in several studies as the peak period of off-shelf freshwater transport (Castelao et al. 2019; Gou et al. 2021; Majumder et al. 2021). In an ocean model with a horizontal spacing of 2.5 km, winds drove the off-shelf transport of meltwater at the shelf break (500–1000 m), while the large-scale circulation and eddies advected the meltwater farther into the deep basin (Castelao et al. 2019). A comparison of 1/12° and 1/4° simulations showed that polar water is exported out of the boundary current system along the West Greenland Shelf in both simulations, with a significant increase in the amount of polar water transported offshore at higher resolution (Pennelly et al. 2019). The pathways and spread of meltwater specifically in the subpolar North Atlantic have been explored with ocean models using passive tracers. In a pair of ocean simulations where mesoscale eddies were either explicitly resolved or parameterized, Dukhovskoy et al. (2016) found that in the simulation with parameterized eddies, the transport of meltwater into the interior basin was lower.

The pathways of meltwater from specific portions of the GIS have also been explored. Luo et al. (2016) estimate that 50%–60% of runoff from southeast Greenland enters the northern Labrador Sea in a 2.5-km eddy-resolving ocean model. This is consistent with Gillard et al. (2016) who found that meltwater from West Greenland tends to enter Baffin Bay, while melt from East Greenland generally enters the Labrador Sea. Similarly, the results from a noneddying 2.4° ocean model showed that the AMOC is most sensitive to the addition of meltwater on the East Greenland continental shelf (Yu et al. 2016). While these studies have addressed how the regional distribution of GIS meltwater impacts its pathways, the role of the vertical distribution has not been clearly addressed.

Glacial fjords connect the GIS to the continental shelf and are locations where both solid discharge and liquid runoff can enter the ocean. In general, fjords are long (50–100 km), narrow (5–10 km), and deep (hundreds of meters), but each has a unique geometry that is important for its dynamics (Straneo and Cenedese 2015; Carroll et al. 2016). As a result of the multitude of mixing processes within fjords, ice sheet runoff is modified before it is exported out of the fjord producing a water mass typically referred to as "glacially modified water." Observations from Beaird et al. (2018) show that glacially modified water exported from Sermilik fjord was comprised of 88% Atlantic Water (see also Beaird et al. 2015, 2017) and that this water mass was observed in the upper 200 m of the fjord (Beaird et al. 2018). Icebergs that calve off the front of

the glacier terminus also distribute meltwater at depth as they melt within fjords (Moon et al. 2018). All these processes are unresolved within global models and not accounted for when meltwater is added to just the surface of the ocean model.

In this paper, we investigate the impact of the vertical mixing of GIS meltwater on the circulation and stratification at the West Greenland Shelf break, which leads to changes in mesoscale eddy generation and the amount of salt fluxed into the Labrador Sea. Mesoscale features must be explicitly represented in this region to understand these impacts. To demonstrate how horizontal grid spacing impacts the representation of these features, we first compare global coupled ocean/sea ice simulations without GIS meltwater that are either mesoscale eddy-active (~2–3-km horizontal spacing) or eddy-permitting (~6–7-km horizontal spacing) in the study region. Next, we use the mesoscale eddy-active ocean/sea ice model with two different meltwater release configurations to investigate the changes in the eastern Labrador Sea. We find that vertically distributed GIS meltwater leads to increased baroclinic conversion and a greater volume of meltwater in the eastern Labrador Sea, compared to the case where meltwater is added only to the surface.

Four forced global coupled ocean/sea ice simulations are used in our sensitivity study. In section 2, descriptions of the model setups and GIS meltwater forcing are provided, as well as the definitions of the energy budget terms and cross-shelf fluxes. Results presented in section 3 are subdivided into two parts. In section 3a, there is a comparison of the mean and eddy kinetic energy in the low- and high-resolution cases with no meltwater. In section 3b, we present the changes in the high-resolution simulations with the addition of meltwater with a focus on the upper ocean energetics [section 3b(1)], changes in the eastern Labrador Sea [section 3b(2)], and the vertical structure of baroclinic conversion at the shelf break [section 3b(3)]. We conclude with a summary and discussion of our results.

2. Methods

In this section, the experimental design used to investigate the sensitivities of the regional ocean circulation to increased horizontal and vertical resolution and the vertical distribution of GIS meltwater is explained. Configuration details of the atmospheric-reanalysis forced global ocean/sea ice simulations used in the study are provided first, the rationale for and details of the sensitivity runs are explained next, and last, the formulations used in the sensitivity analyses are introduced.

a. Model description

Four forced global ocean/sea ice simulations were produced using the Energy Exascale Earth System v0-HiLAT (E3SMv0-HiLAT; Hecht et al. 2019) model, which utilizes the Parallel Ocean Program 2 (POP2; Dukowicz and Smith 1994) for the ocean component and the Community Ice Code, version 5 (CICE5; Hunke et al. 2010), for the sea ice component. The HiLat code is a derivative of the Community Earth System Model, version 1 (Hurrell et al. 2013). The corrected interannually varying Co-ordinated Ocean–Ice Reference Experiment-II corrected interannual forcing (CORE-202 II CIAF; Large and Yeager 2009) fluxes from 1970 to 2009 were used for the atmospheric forcing. The sea surface salinity (top 10 m) was relaxed toward the Polar Science Center Hydrographic Climatology 3.0 (PHC 3.0; Steele et al. 2001) with a very weak 4-yr restoring time scale to limit model drift. The model bathymetry was produced using the 30-arc-s General Bathymetric Chart of the Oceans (GEBCO; Weatherall et al. 2015) product.

Three of the four simulations were configured to be globally mesoscale eddy-active in ocean basins by using an "ultra-high" horizontal resolution tripolar grid that has a horizontal spacing of 8 km at the equator reducing to 2 km at the poles referred to as the UH8to2 grid. The Northern Hemisphere poles are located in Siberia and Greenland, resulting in a horizontal spacing of ~2–3 km over the Greenland continental shelf. POP2 uses z-level coordinates; the UH8to2 consists of 60 vertical levels that are nonuniformly spaced with thicknesses of 10 m in the upper 160 and 250 m close to the ocean floor; the maximum depth is 5500 m. Partial bottom cells (PBCs) are used to more smoothly represent the ocean bathymetry.

The fourth simulation is largely an analogous E3SMv0-HiLAT simulation but is on a 0.1° tripolar grid, with a horizontal spacing of ~6–7 km in the western subpolar North Atlantic. Unlike UH8to2, the 0.1° tripolar grid does not have a pole in Greenland; the poles are in North America and Asia. This simulation has 42 nonuniform vertical levels with 10-m thickness at the surface and 250 m at depth, and PBCs are used. This simulation is referred to as CTRL01 and was run from 1970 through 2009.

The ocean component of the UH8to2 simulations was initialized from a 2-month stand-alone POP2 integration, which, in turn, was initialized from rest, using potential temperature and salinity from the PHC 3.0 (Steele et al. 2001). The sea ice was initialized using 2-m uniformly thick sea ice, with the ice edge defined by the January climatological mean from satellite (Special Sensor Microwave Imager) observations. For the 0.1° simulation, the ocean was initialized from a 17-day stand-alone POP2 run forced with CORE-II CIAF, and the sea ice initial condition was the same as that used in the UH8to2 except interpolated onto the 0.1° grid. The 0.1° configuration was spun up from 1970 to 1990, while the UH8to2 configuration was spun up from 1975 to 1990; the availability of computer resources dictated the shorter UH8to2 spinup period. Beginning in 1990, land-ice melt fluxes were added to the ocean.

Representations of land-ice melt were included in the two UH8to2 simulations, both around the Greenland continental shelves and in the Southern Ocean. For the GIS, solid discharge and liquid runoff from Bamber et al. (2018) were added. To create this product, Bamber et al. (2018) obtained monthly time series of the liquid runoff from output produced by a regional climate model (RACMO2.3p2) forced with atmospheric reanalyses (ERA-40 and ERA-Interim) (Noël et al. 2018). They derived solid ice fluxes from on-ice thickness (Morlighem et al. 2017) and surface ice velocities from satellite-based observations. For the period 1992–2010, they produced annual values; for years without observations, correlations between time-averaged runoff and discharge were used to estimate discharge. We consider both the solid discharge and

liquid runoff from the GIS to be meltwater and treat these terms in the same way. Since the CORE-II CIAF forcing does not include an explicit representation of the meltwater from the GIS, we masked out any river runoff associated with this forcing over Greenland (Large and Yeager 2009; Dai and Trenberth 2002) and replaced it with the tundra runoff component from Bamber et al. (2018), which is analogous to the CORE-II river runoff. During the spinup period, neither meltwater nor tundra runoff was added to the ocean model. See the online supplemental material for details on the Antarctic Ice Sheet fluxes added to the Southern Ocean.

The meltwater forcing was applied via a virtual salt flux and had no associated thermal forcing. Using virtual salt fluxes in an ocean model is a fundamentally nonphysical means of applying freshwater fluxes. Where implemented, salt is either removed from or added to the ocean in a specified amount. This does not impact the total volume of the ocean and depends on a reference salinity, which can lead to the misrepresentation of freshwater fluxes in low salinity regions (Yin et al. 2010). However, Yin et al. (2010) showed that for the present climate state and relatively small freshwater fluxes, virtual salt flux and real freshwater flux models were similar. Throughout this study, we refer to meltwater being added to the ocean but acknowledge that with a virtual salt flux model, there was no real volume flux, and the forcing was just removing salt.

b. *Experimental design*

1) Resolution sensitivity

Mesoscale eddies are key contributors to the dynamics of the Labrador Sea (Chanut et al. 2008). The scale of these eddies varies from large Irminger Rings (30–60 km) (Lilly et al. 2003) to much smaller boundary current (~10 km) and convective eddies (10–35 km) (Eden and Böning 2002; Brandt et al. 2004; Chanut et al. 2008; Marshall and Schott 1999; Rieck et al. 2019). The smallest of these eddy length scales is comparable to the estimated first baroclinic Rossby radius (~8–10 km) in the deep Labrador Sea (Eden 2007; Funk et al. 2009).

The largest mesoscale eddies in the global ocean can be hundreds of kilometers in size. If the horizontal grid spacing is half that of the first baroclinic Rossby radius in the deep ocean, eddies with a horizontal scale of the first baroclinic Rossby radius are minimally resolved. Models of this resolution are often referred to as "eddy-resolving." If the horizontal grid spacing is greater than half that of the first baroclinic Rossby radius and no more than ~100 km, the model resolution is described as "eddy-permitting" in the deep ocean. When the model resolution is greater than ~100 km, it is insufficient to resolve or permit eddies, so eddies and associated eddy processes must be parameterized (Gent and Mcwilliams 1990; Mana and Zanna 2014).

Global ~1/10° grids are increasingly being used in coupled climate models (Roberts et al. 2020). In the Labrador Sea, the necessary horizontal spacing to be eddy-permitting in the deep ocean is ~1/10° (Funk et al. 2009; Hallberg 2013). The horizontal spacing of the UH8to2 grid is generally less than half the estimated first baroclinic Rossby radius in the deep ocean; consequently, the UH8to2 explicitly represents smaller scale features than the ~1/10°. To appreciate the differences in the simulated WGC system when these smaller scale features are resolved, we compare the ~1/10° and the UH8to2 simulations. These simulations are designated CTRL01 and CTRL, respectively. Neither run includes meltwater. These comparisons provide a context for the interpretation of the UH8to2 sensitivity results that include meltwater representations.

2) Greenland meltwater forcing

To assess the sensitivity to the vertical distribution of meltwater from the GIS within glacial fjords, we performed two experiments with the UH8to2 configuration. The GIS fluxes from Bamber et al. (2018) used in these experiments were remapped from their original 5-km grid onto the nearest UH8to2 ocean grid point. A horizontal Gaussian filter with a length scale of ~14 km (a quarter of a degree of latitude at 60°N) was applied to distribute the meltwater horizontally. This length scale is roughly twice the first baroclinic Rossby radius in the region and was used to represent the unresolved alongshore plumes of freshwater. In addition, horizontal spreading was necessary to distribute meltwater offshore such that meltwater was added to areas deep enough to allow the meltwater to be vertically distributed. A mask was used to ensure that meltwater was not added in regions deeper than 400 m in order to keep the meltwater confined to the shelf. Finally, the total volume of meltwater was rescaled after the mask was applied to ensure that the net amount agrees with the amount specified by the dataset (Bamber et al. 2018). A dye tracer was added proportionally to the volume of meltwater added and was used to track the spread of meltwater throughout the simulation. See the supplemental material for a map of the horizontal distribution of the meltwater released around the continental shelf and a schematic representation of its vertical distribution.

Two different vertical distributions of meltwater were tested in the UH8to2 configuration both branched off the UH8to2 spinup (1975–90). The "Spread Case" or SPRD was run from 1990 through 2009. In SPRD, runoff from the GIS was vertically distributed uniformly over the upper 200 m of the water column. In contrast, in the "Surface Case" or SURF, as in previous Greenland meltwater perturbation studies, all runoff was added to the surface layer of the model (10 m). The SURF was run from 1990 to 1993. In both SURF and SPRD simulations, tundra runoff, which is analogous to riverine runoff, was added to the surface layer of the model. SPRD and SURF have the same total volume of land-ice meltwater forcing. The UH8to2 spinup run was continued from 1990 to 1992 with no meltwater added; it is the UH8to2 Control (CTRL) simulation discussed earlier.

Only short periods are available for intercomparison among the UH8to2 simulations, and only 1992 can be compared among the three cases. The very high computational cost of running the UH8to2 model precluded us from running multiple simulations for more years. The years used for intercomparison are in the early 1990s, when runoff from the GIS was relatively low (see Bamber et al. 2018). Furthermore,

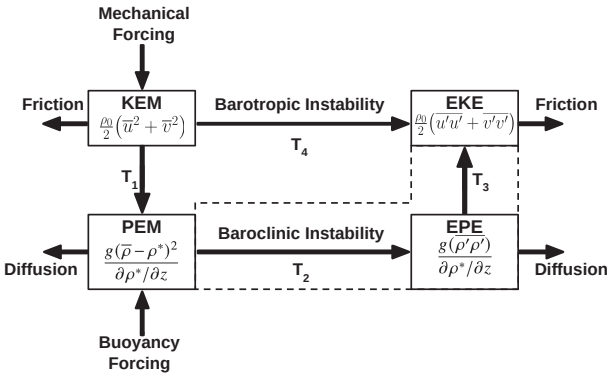

FIG. 2. Diagram showing the components of the oceanic energy budget, after Böning and Budich (1992). The definitions for the KEM, EKE, PEM, and EPE are given in the boxes; definitions for the eddy and mean decomposition are given in section 2c. The energy conversion terms representing barotropic instability (T_4) and baroclinic instability (both T_2 and T_3, as indicated by the dashed box) are also labeled.

both the winters of 1992/93 and 1993/94 were during the relatively strong positive phase of the North Atlantic Oscillation (NAO) (Pickart et al. 2002). As we are comparing simulations with the same atmospheric state, not capturing the full variability of the NAO may not limit our ability to understand the sensitivity of the ocean to the vertical distribution of meltwater.

c. *Energy conversion and flux formulations*

A key goal of our study is to investigate how explicitly resolving mesoscale eddies and including GIS meltwater impacts the flux of salt off the West Greenland continental shelf. In this section, we introduce the definitions used to calculate the energy conversion terms and cross-isobath fluxes.

Following the approach of Böning and Budich (1992) and Beckmann et al. (1994), the terms of the energy budget are defined using quasigeostrophic assumptions, namely, that horizontal density gradients are much less than the stratification and that the contribution of the vertical velocity to kinetic energy can be neglected. The transport of energy into a control volume is not calculated; thus, we do not aim to close the energy budget or describe the complete energy cycle. Similar decompositions of the energy cycle have been carried out using other primitive equation models (e.g., Böning and Budich 1992; Eden and Böning 2002; Trodahl and Isachsen 2018; Rieck et al. 2019; Stewart et al. 2019).

A diagram of the ocean energy cycle is shown in Fig. 2, which illustrates the sources (mechanical and buoyancy forcing) and sinks (friction and diffusion) of energy as well as the conversions between mean and eddy components. The mean kinetic energy (KEM) is converted to EKE through barotropic instabilities; the transfer between these two terms more generally represents the work of the Reynolds stresses against the mean shear (Böning and Budich 1992). Buoyancy forcing, such as the addition of meltwater, influences the mean available potential energy (PEM), which can be converted to eddy available potential energy (EPE) through baroclinic conversion. The conversion of EPE to EKE is also related to the generation of baroclinic instabilities. While the arrows on the diagram point in only one direction, energy can also be transferred from eddy to mean components. We use energy densities so that the components of the budget have consistent units.

To calculate the mean and eddy terms, we consider only temporal anomalies. The eddy component of the zonal velocity is defined as $u' = u - \overline{u}$, where $\overline{u}$ is the annual average of u and the daily averaged zonal velocity is u. The mean and eddy components of the meridional velocity are similarly calculated. The potential density, referenced to the surface, ρ is similarly decomposed into mean and eddy terms: $\rho' = \rho - \overline{\rho}$. A reference density profile $\rho^*(z)$ is used to define the available potential energy. Therefore, the energy density terms in the boxes of Fig. 2 can be defined as

$$\mathrm{KEM} = \frac{\rho_0}{2}(\overline{u}^2 + \overline{v}^2), \tag{1}$$

$$\mathrm{EKE} = \frac{\rho_0}{2}(\overline{u'u'} + \overline{v'v'}), \tag{2}$$

$$\mathrm{PEM} = \frac{1}{2}\frac{g(\overline{\rho} - \rho^*)^2}{\partial\rho^*/\partial z}, \tag{3}$$

$$\mathrm{EPE} = \frac{1}{2}\frac{g(\overline{\rho'\rho'})}{\partial\rho^*/\partial z}, \tag{4}$$

where $\rho^*(z)$ is the temporally and horizontally averaged potential density.

For a closed volume, we can quantify the transfer terms in the energy budget as

$$T_1 = g\int\int\int \overline{w}\overline{\rho}\, dx\, dy\, dz, \tag{5}$$

$$T_2 = -\rho_0\int\int\int \left(\frac{g}{N\rho_0}\right)^2\left(\overline{u'\rho'}\frac{\partial\overline{\rho}}{\partial x} + \overline{v'\rho'}\frac{\partial\overline{\rho}}{\partial y}\right)dx\, dy\, dz, \tag{6}$$

$$T_3 = -g\int\int\int \overline{w'\rho'}\, dx\, dy\, dz, \tag{7}$$

$$T_4 = -\rho_0\int\int\int \left[\overline{u'^2}\frac{\partial\overline{u}}{\partial x} + \overline{u'v'}\left(\frac{\partial\overline{u}}{\partial y} + \frac{\partial\overline{v}}{\partial x}\right) + \overline{v'^2}\frac{\partial\overline{v}}{\partial y}\right]dx\, dy\, dz. \tag{8}$$

A reference density of $\rho_0 = 1025$ kg m^{-3} is used, and N^2 is the annual mean Brunt–Väisälä frequency, which is given as follows:

$$N^2 = -\frac{g}{\rho_0}\frac{d\rho^*}{dz}. \tag{9}$$

Without a complete energy budget, these terms can provide only a qualitative insight into the mechanisms of energy conversion.

One important component of PEM, EPE, and T_2 is the choice of a reference density profile $\rho^*(z)$. For our study region, we tested the sensitivity of these metrics to the choice of

$\rho^*(z)$ by using the density profile along the shelf break or using the mean profile within the Labrador and Irminger Seas. To find the density along the shelf break, we used our defined shelf-break contour. For the Labrador and Irminger Seas we defined a region deeper than 2500 m, north of 55°N and east of the Reykjanes Ridge. The density at the shelf break changes significantly with the addition of meltwater; therefore, when used as a reference profile for calculating PEM, this profile produces results that suggest PEM changes greatly between CTRL and SPRD far from where the impacts of meltwater would be expected in the relatively short period of our simulation. When the CTRL shelf profile was used for all cases, this change was reduced, indicating that the choice of $\rho^*(z)$ was the source of the difference. The stratification in the Labrador and Irminger Seas does not change as significantly between the UH8to2 cases. Using the basin-wide ρ^* profile provides more consistent comparisons across cases while still using a density profile appropriate to each case.

In addition to the energy budget terms, we calculate the salt and meltwater convergence in the Labrador Sea. We define a control volume for the eastern Labrador Sea shown in Fig. 1. The boundary of this control volume is based on the faces of the model grid cells. To calculate the salt and meltwater tracer fluxes offline, we use instantaneous fields saved on the first day of each month (restart files). This is to avoid the error introduced from temporally averaging eddying processes and other high-frequency variability.

The salt flux across a defined contour is given by

$$F_S = \int_H^0 \int_0^L S(x, z)\hat{v}\, dx\, dz, \tag{10}$$

where S is the salinity along the contour. The along-shelf direction is x and $\hat{v}$ is the cross-contour velocity, H is the depth, and L is the length along the contour. The positive direction is defined as into the basin; positive fluxes indicate the volume flux into the Labrador Sea. We choose to use a salt flux rather than a freshwater flux to avoid the ambiguity associated with choosing a reference salinity (Schauer and Losch 2019). A dye tracer is added proportionally to the virtual salt flux and has units of grams per kilogram. We can calculate the flux of this tracer as

$$\mathrm{MWT} = \int_H^0 \int_0^L \mu(x, z, t)\hat{v}\, d\hat{x}\, dz, \tag{11}$$

where μ is the dye tracer concentration. The salt or meltwater convergence in a closed volume is calculated by integrating the flux around the entire boundary.

Because the dye tracer being added to the ocean is proportional to the virtual salt flux, the dye tracer concentration can be converted to a meltwater content by inverting the conversion of meltwater volume flux to virtual salt flux as is done by POP2. The meltwater content is unitless and indicates the fraction of the volume of a model grid cell consisting of meltwater. It is defined as

$$\mathrm{MWC} = \frac{\mu}{\rho_{\mathrm{FW}}\, S_{\mathrm{ref}}\, \mathrm{FWF}_{\mathrm{factor}}}, \tag{12}$$

where ρ_{FW} is the density of freshwater (1000 kg m^{-3}) and $\mathrm{FWF}_{\mathrm{factor}} = 1 \times 10^{-5}$ m^3 kg^{-1}. The freshwater flux factor is a constant defined within POP2 to rescale the volume of freshwater flux.

3. Results

In this section, we first compare the mean and eddy kinetic energy in the low- and high-resolution ocean/sea ice simulations with no meltwater to highlight the features of the WGC system that are better represented in the UH8to2 simulations. Next, we present the upper ocean energy budget terms, cross-shelf flux, and Labrador Sea properties from the UH8to2 simulations. To understand the impacts of meltwater on the shelf break, we examine the vertical structure of the meltwater fluxes and baroclinic conversion at the shelf break in the high-resolution meltwater forcing simulations.

a. *Comparison of resolution sensitivity experiments*

The dependence of the strength and positioning of the WGC and West Greenland Coastal Current (WGCC) along with local eddy shedding variability on horizontal and vertical grid spacing is assessed by comparing the spatial maps of the kinetic energy budget terms: KEM and EKE [Eqs. (1) and (2)] from CTRL01 and CTRL simulations (Fig. 3). These terms are vertically integrated over the upper 230 m of the water column (where the direct impacts of the meltwater forcing occur) and averaged over 1992. The potential energy terms are presented in the supplemental material. Difference fields (CTRL minus CTRL01) for each of the terms are also provided in which CTRL01 is interpolated onto the UH8to2 model grid. The West Greenland shelf-break contour is shown in black (northern shelf break) and white (southern shelf break). A box delineating the area of regional high EKE in the high-resolution simulations is plotted; the boundaries of this box extend from 60° to 62.5°N and 50° to 55.5°W.

The KEM of CTRL01 and CTRL simulations is shown in Figs. 3a and 3b, along with their difference in Fig. 3c. Along the entire shelf break, the WGC is narrower and its core stronger in CTRL compared to CTRL01. At lower resolution, the on-shelf WGCC is weaker. The WGCC crosses the northern part of the shelf-break contour in CTRL, but because this current is represented farther off the shelf in CTRL01, it does not cross the shelf-break contour in CTRL01. There are four troughs in the UH8to2 bathymetry that are not present in CTRL01 along the northern shelf break, which may contribute to the difference in the position of the WGCC. The vertical structure of these currents at the locations of the O-SNAP arrays at Cape Farewell is shown in the supplemental material.

The EKE of CTRL01 and CTRL simulations is plotted in Figs. 3d and 3e and their difference in Fig. 3f. In CTRL01 simulation, the locus of high EKE is close to the shelf break between the 2000- and 3000-m isobaths. The patch of elevated EKE does not extend south into the interior Labrador Sea (deeper than the 3000-m isobath) but extends further west. In CTRL, the area of EKE above 60 kg m^{-1} s^{-2} is more expansive. The average EKE within the defined box in CTRL01 simulation

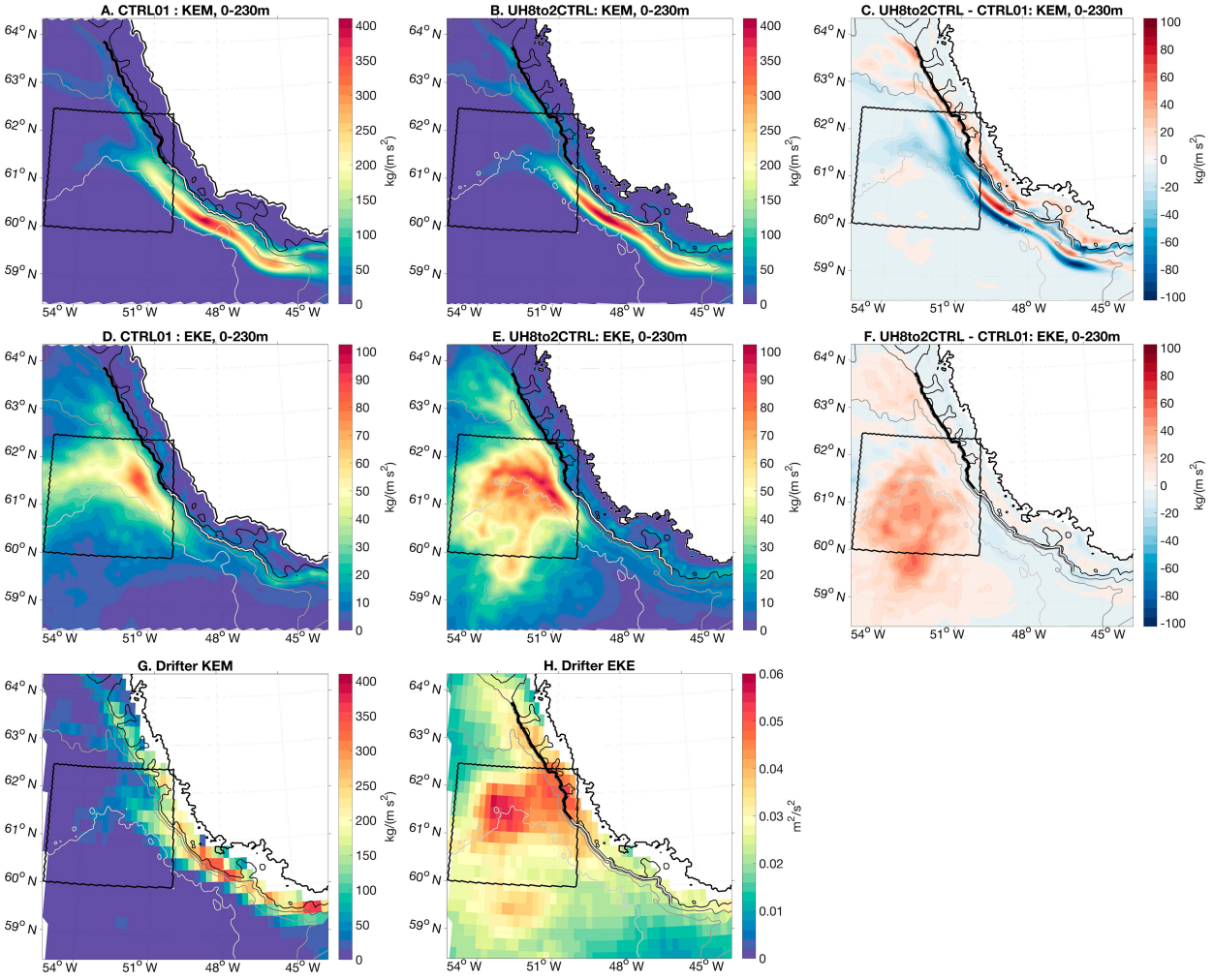

FIG. 3. (a)–(f) Average (1992) KEM and EKE for CTRL01 and CTRL, and (g),(h) their difference (CTRL minus CTRL01) averaged over the upper 230 m. The CTRL01 is interpolated onto the UH8to2 grid in order to calculate the difference. The shelf-break contour is shown by the white (southern shelf break) and black (northern shelf break) lines. The 200-, 800-, 2000-, and 3000-m isobaths are plotted from dark to light gray. The black box indicates the high EKE region in the high-resolution simulations. Estimates of (g) speed and (h) EKE from 15-m drogued and undrogued drifters (Laurindo et al. 2017) are provided for qualitative comparison.

(Fig. 3d) is 28.2 kg m^{-1} s^{-2} compared to 49.1 kg m^{-1} s^{-2} in CTRL (Fig. 3e). This amounts to a 74% increase in the average EKE in that region when using the UH8to2 grid. A second region of elevated EKE along the West Greenland shelf break, between 62.5° and 64°N, is also more energetic in CTRL simulation compared to CTRL01.

We can qualitatively compare the simulations to climatologies (1979–2015) of KEM (Fig. 3g) and EKE (Fig. 3h) based on velocities from 15-m drogued and undrogued satellite-tracked surface drifters available from the Atlantic Meteorological and Oceanic Laboratory of the National Oceanic and Atmospheric Administration (Laurindo et al. 2017). These data are available on a grid; regions with fewer than 90 drifter days per unit area are not shown. Because of the low resolution of the drifter derived speed, it is challenging to compare to the resolved currents in either CTRL or CTRL01. Nonetheless, observed KEM shows a strong mean flow near Cape Desolation over the shelf slope similar to CTRL. Both the models and observations show the three locations where the WGC branches away from the shelf break. The southward extension of high EKE in CTRL simulation is qualitatively much more similar to the estimate of the observed EKE shown here than CTRL01.

As expected, CTRL has more narrower more defined representations of the WGC/WGCC and more realistic region of elevated EKE in the Labrador Sea compared to CTRL01. Both the shelf-break currents and eddies play an important role in the flux of meltwater along the Greenland Shelf and into the basin. Because our results depend on explicitly representing these small-scale features, these findings may not be reproducible in simulations with resolutions similar to CTRL01.

b. *Comparison of Greenland meltwater forcing experiments*

1) UPPER OCEAN ENERGETICS

To understand sensitivity to both the addition of meltwater and the structure of meltwater distribution around Greenland in an eddy-active ocean model, we compare the components of the energy budget on the shelf and in the Labrador basin in the high-resolution simulations. Figure 4 shows the difference in the 1992 average energy budget terms in the upper 230 m of the meltwater perturbation experiments relative to CTRL (Fig. 3 and supplemental Fig. 6). To establish where these changes are robust, we calculate monthly averages for each term of the energy budget [Eqs. (1)–(4)], providing 12 estimates of the energy budget terms. We assume that these estimates are independent and use them to calculate the standard-error-of-the-mean for each budget term at every location. We consider the difference to be statistically significant where the difference between two cases is greater than $2\sqrt{(\sigma_1^2 + \sigma_2^2)/2}$, where σ_1 and σ_2 are the standard errors of the mean in the two cases (regions without hatching in Fig. 4). In the next paragraphs, the kinetic and potential energy terms are described in more detail; the PEM maps are included in the supplemental material only.

The change in the kinetic energy terms (KEM and EKE) with the addition of meltwater is small compared to the standard deviation but suggests an increase in the energy of the WGC system. The maps of differences in KEM: SURF minus CTRL in Fig. 4a and SPRD minus CTRL in Fig. 4b, reflect the increase in the speed of the coastal currents with the addition of meltwater. The increase in KEM with the addition of meltwater in SPRD (Fig. 4b) occurs across both the WGC and WGCC. Only the increase in KEM in the core of the WGC is significant in SURF and SPRD; there, KEM increases by 10%–20% in SPRD. The increase in the KEM of the WGCC is significant along the southern shelf in SPRD but not SURF, and the increase in the energy is smaller compared to the increase in the WGC.

Similar to the KEM, in many regions the change in the EKE with the addition of meltwater is not significant compared to the estimated standard error of the mean (Figs. 4c,d). In part, this is because the period over which the EKE is averaged is comparable to the length of time that Irminger Rings can persist in the Labrador Sea (1–2 years). The SURF and SPRD have an average EKE of 51.7 and 52.2 kg m^{-1} s^{-2}, respectively, in the box compared to 49.1 kg m^{-1} s^{-2} in CTRL. The volume-averaged EKE results suggest an increase in the EKE overall with the addition of meltwater. In the northern part of the box, EKE is greater with the addition of meltwater (Figs. 4c,d) but is often not greater than the standard deviation. This possibly indicates a northward shift in the region of elevated EKE, which would require a longer time series to be established.

For each UH8to2 simulation, the horizontally averaged density $\rho^*(z)$ within the Labrador and Irminger Seas is used to calculate the potential energy terms. Therefore, before describing the potential energy terms, we must first examine its differences among the UH8to2 simulations. The corresponding maximum buoyancy frequency (N) of this density profile in CTRL is 4.8×10^{-5} s^{-1}, SPRD is 4.8×10^{-5} s^{-1}, and SURF is 4.9×10^{-5} s^{-1}; in all cases, the maximum stratification is at 35 m. In the near-surface layer (0–40 m) of CTRL, the potential density is 1027.46 kg m^{-3}, while SPRD has the lightest surface layer of all the UH8to2 simulations with a minimum density of 1027.45 kg m^{-3}. Changes in the near-surface density and stratification with the addition of meltwater are also indicators of the potential sensitivity of deep convection sites in the subpolar North Atlantic to meltwater from the GIS.

EPE differences between the UH8to2 simulations for 1992 in the upper 230 m are shown in Figs. 4e and 4f, respectively. Because the reference profile is defined by the basin density, there will always be more available energy on the shelf than in the basin. The stratification on the shelf is also most changed by the addition of meltwater, therefore that is where both SPRD and SURF show the largest changes in the EPE. With the addition of meltwater, the EPE increases on the shelf and in the northern high EKE zone. Closest to the coast and especially on the northern part of the shelf, SURF and SPRD both have roughly 50% more EPE compared to CTRL. While the difference in the northern high EKE zone is small, it is spatially coherent and greater than the standard deviation, suggesting the increase to be robust.

The addition of vertically distributed meltwater in the upper ocean of SPRD results in faster mean currents, possibly an increase in the EKE, and an increase in the EPE particularly along the northern shelf. However, meltwater only directly modifies ocean salinity, which from the perspective of the ocean energy budget translates only to changes in the PEM. We examine the energy conversion terms to better understand the mechanisms that convert a change in PEM to energy in other components of the ocean energy budget. We focus on the baroclinic and barotropic energy conversion terms because they show the most robust changes with the addition of meltwater. The other two energy conversion terms (T_1 and T_3) were not significantly impacted by the addition of meltwater in most of this region; therefore, those fields are shown only in the supplemental material.

The 1992 average baroclinic and barotropic energy conversion terms in the upper 230 m of the high-resolution simulations are shown in Fig. 5. The baroclinic conversion term T_2 is primarily positive along the shelf break, indicating baroclinic conversion (PEM to EPE; Figs. 5a–c). The strength of the baroclinic conversion is nonuniform and indicates a strong dependency on bathymetry. However, overall SURF and SPRDs have higher positive values over the continental shelf relative to CTRL. The barotropic conversion T_4 (KEM to EKE) is greater than baroclinic conversion off the shelf and has a distinct spatial pattern that is robust across the UH8to2 cases (Figs. 5d–f). There are three "hotspots" of barotropic conversion off the shelf oriented parallel to the shelf break and extend from ~60° to 61.5°N, ~62° to 63°N, and ~63° to 64°N. The southernmost patch is the strongest, straddles the eastern edge of the high EKE box, and is located in the same area as a region of elevated baroclinic conversion off the shelf. This could be a key location of eddy formation through both baroclinic and barotropic conversion.

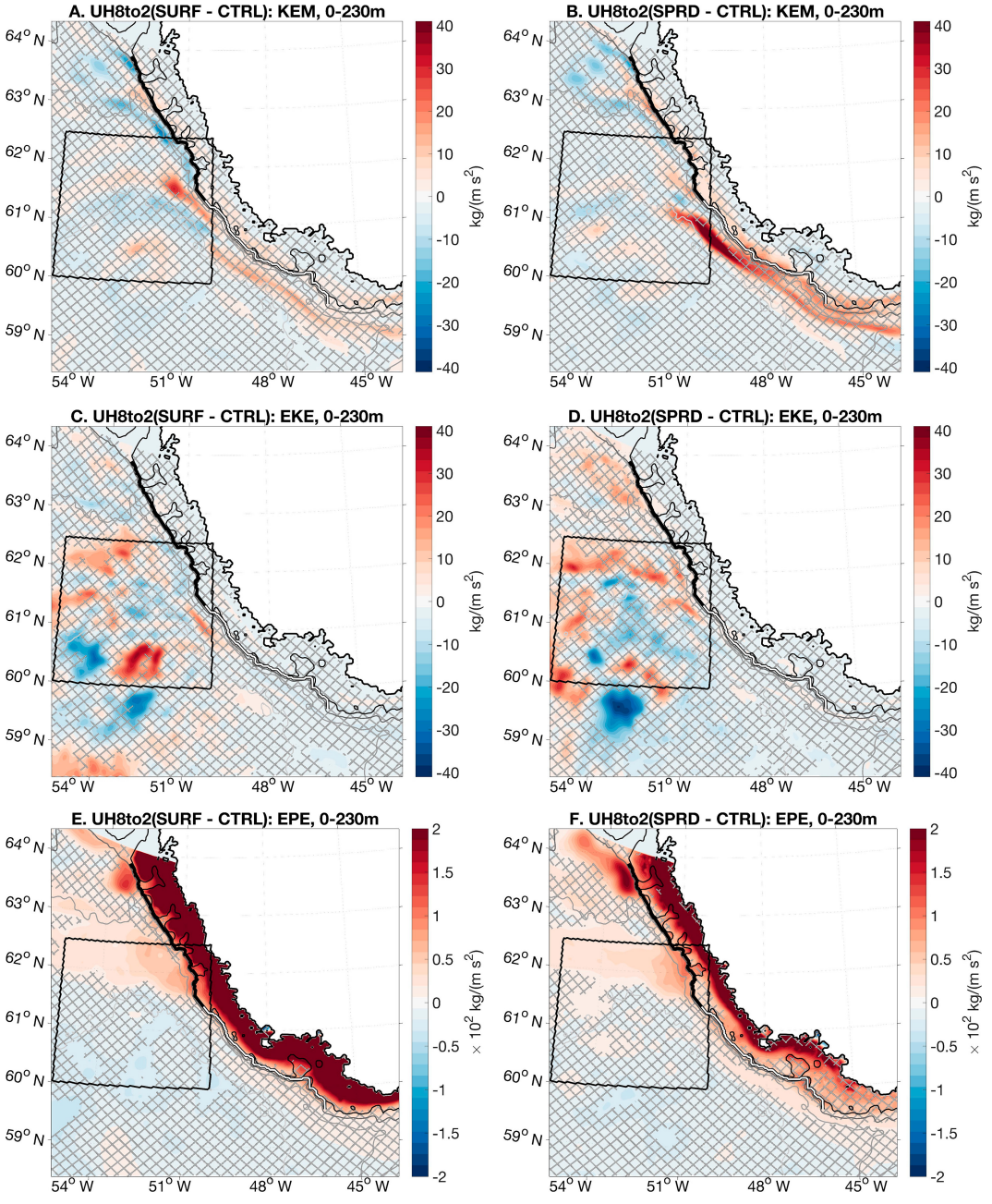

FIG. 4. Average (1992) difference in energy budget terms (KEM, EKE, and EPE) for (a),(c),(e) SURF minus CTRL and (b),(d),(f) SPRD minus CTRL averaged over the upper 230 m. Hatched areas show where the difference was less than $2\sqrt{(\sigma_1^2 + \sigma_2^2)/2}$, where σ is the standard deviation of the monthly averages of the energy budget term in the high-resolution simulations. The shelf-break contour is shown by the white (southern shelf break) and black (northern shelf break) lines. The 200-, 800-, 2000-, and 3000-m isobaths are plotted from dark to light gray. The black box indicates the high EKE region in the high-resolution simulations.

To identify changes in baroclinic and barotropic conversion arising from the addition of meltwater, we compare the average (1992) energy difference in conversion terms for CTRL, SURF, and SPRD averaged over the upper 230 m (Fig. 6). With the addition of meltwater, T_2 increases over nearly the entire shelf and shelf break (Figs. 6a,b). In addition, the baroclinic conversion hotspots located along the northern shelf break strengthen. In section 3b(3), the vertical structure of this increase at the shelf break is explored in more detail. In addition, there is an increase in T_2 at ~61.5°N extending from the shelf break into the high EKE box in both SPRD and SURF. Since the meltwater forcing directly modifies the potential energy of the system, not the

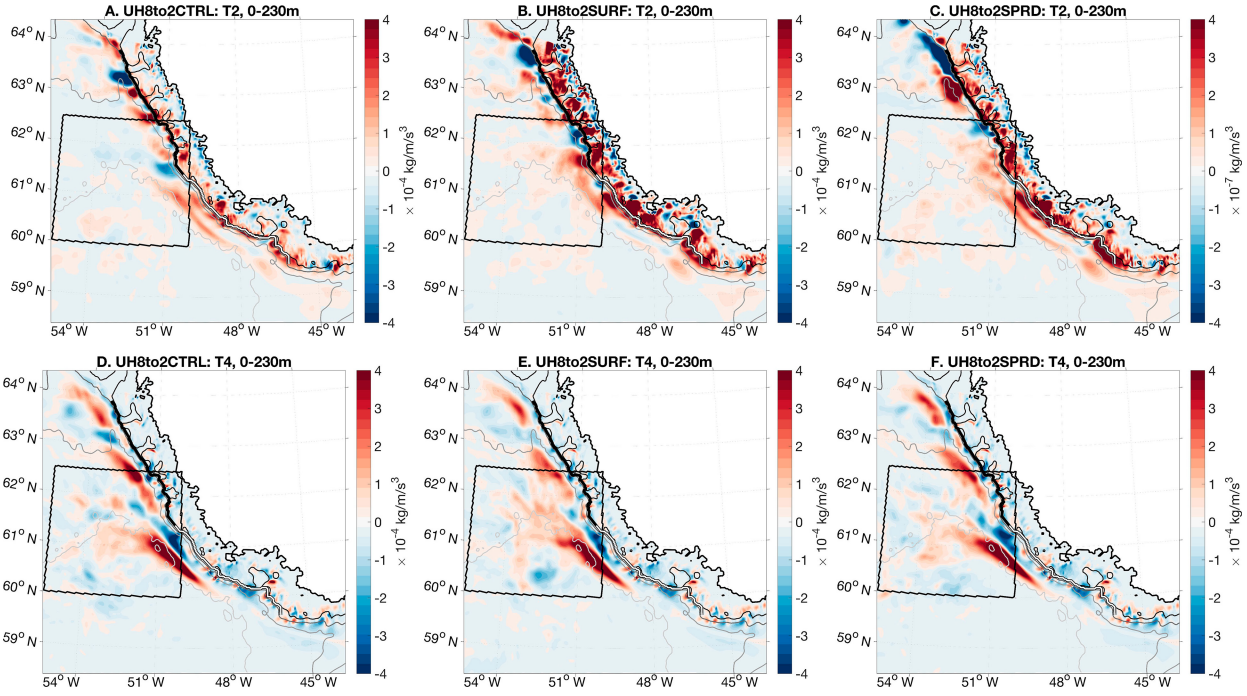

FIG. 5. Average (1992) energy conversion terms (T_2 and T_4) for (a),(d) CTRL, (b),(e) SURF, and (c),(f) SPRD averaged over the upper 230 m. All the energy conversion terms for CTRL, SPRD, and SURF are plotted in the supplemental material. The shelf-break contour is shown by the white (southern shelf break) and black (northern shelf break) lines. The 200-, 800-, 2000-, and 3000-m isobaths are plotted from dark to light gray. The black box indicates the high EKE region.

kinetic energy, we expect a less clear response to the forcing in T_4, which converts KEM to EKE. Indeed, the changes in T_4 (Figs. 6c,d) do not show a simple change in the three hotspots previously described. The area with a significant difference is mostly within the high EKE region where SPRD has a net decrease while SURF shows a net increase. These changes could be due to internal variability rather than the impact of meltwater.

2) SALT AND MELTWATER IN THE LABRADOR SEA

A key focus of this study is to understand freshening impacts in the Labrador Sea arising from the GIS meltwater representations. Differences in the pathways of meltwater can be ascertained by comparing the vertically integrated meltwater content [Eq. (12)]. Figure 7 shows the vertically integrated meltwater content in December 1993, the end of the meltwater forcing experiment comparison period, for SURF and SPRD. As has been shown in previous modeling experiments, both simulations show an accumulation of meltwater in Baffin Bay (Gillard et al. 2016). Spreading of meltwater into the subpolar gyre occurs near the Flemish Cap, similar to subpolar meltwater spreading in the high-resolution experiments by Böning et al. (2016). A notable difference between our two simulations is the meltwater content in the eastern Labrador Sea, particularly in the highly eddy-active region (Figs. 7c,d, black box). To quantify the difference, we calculate the convergence of salt and dye in a control volume in the eastern Labrador Sea that encompasses much of the West Greenland slope and extends offshore into the deep Labrador basin (see Fig. 1).

The convergence of salt and meltwater is shown in Figs. 8a and 8b; positive values indicate convergence within the control volume, while negative values indicate divergence. There is a net convergence of salt within the control volume for nearly all months within the comparison period, as reflected in the overall increase in the salinity. In October of 1992, there was a strong divergence of salt across all three experiments; this consistency suggests that the divergence may be driven by the atmospheric forcing. The mean salt convergence in 1992 is 6.8×10^5 m s^{-1} in CTRL, 7.0×10^5 m s^{-1} in SURF, and 1.0×10^6 m s^{-1} in SPRD. The net salt convergence is highly variable and would be impacted by the eddy features present in the instantaneous fields used to calculate the convergence. Furthermore, warm salty inflows from the West Greenland/Irminger Current as well as Irminger Rings enter our control volume and will contribute to positive salt convergence.

We can also quantify the changes to the volume average salinity in the eastern Labrador Sea. The difference in the salinity across experiments in such a large region is small but present. Figure 8c shows the volume average salinity for all UH8to2 experiments. SPRD is consistently fresher than SURF or CTRL, although we acknowledge that the magnitude of this difference is small (approximately 0.003). Furthermore, linear trends in the volume average salinity were calculated but were not significant for any experiment. Although not significant, they possibly suggest that increasing salinification from Irminger Current inflows could be offset by increasing land-ice melt.

For meltwater, there is convergence from September to February and divergence or a weak neutral state for the rest

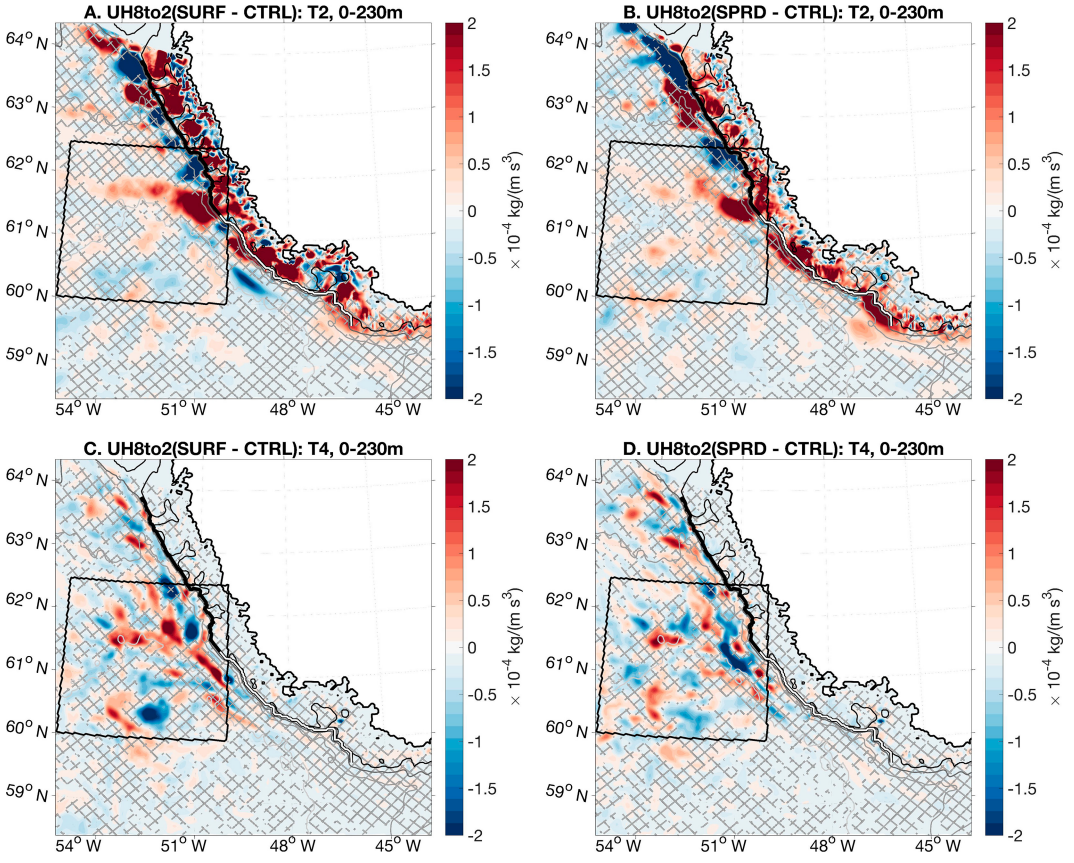

FIG. 6. Average (1992) difference in energy conversion terms (T_2 and T_4) for CTRL, SURF, and SPRD averaged over the upper 230 m. Hatched areas show where the difference was less than $2\sqrt{(\sigma_1^2 + \sigma_2^2)/2}$, where σ is the standard deviation of the monthly averages of the energy conversion term in the high-resolution simulations. All the energy conversion terms for CTRL, SPRD, and SURF are plotted in the supplemental material. The shelf-break contour is shown by the white (southern shelf break) and black (northern shelf break) lines. The 200-, 800-, 2000-, and 3000-m isobaths are plotted from dark to light gray. The black box indicates the high EKE region.

of the year. The dye tracer convergence peaks in the autumn/winter and is weakest in the summer. The average convergence of dye tracer in the Labrador Sea over 1992/93 is 46.5 g kg^{-1} m s^{-1} in SURF and 93.3 g kg^{-1} m s^{-1} in SPRD, indicating dye entering the basin. The time evolution of the integrated meltwater volume is shown in Fig. 8d. The average difference in the meltwater volume is 1.31×10^8 m^3, and there is more meltwater in SPRD than SURF except in March, April, and May of both years when the volume is similar. In both experiments, the maximum volume of meltwater within the basin occurs in winter. Over the 2 years shown here, there is an increase in the meltwater volume within the basin. In SPRD, the trend is approximately 3.8×10^7 m^3 yr^{-1} and, in SURF, it is 13×10^7 m^3 yr^{-1} over this period as indicated by the dashed lines in Fig. 8d. The trend in SURF is not significant but is significant in SPRD.

The difference in dye tracer convergence indicates an overall greater flux of meltwater off the shelf in SPRD. The 1992/93 mean dye convergence is greater in SPRD compared to SURF. The seasonality of the dye tracer flux off the shelf, as shown in Fig. 8, depends both on the seasonal strengthening of the winds which drive off-shelf transport (Schulze Chretien and Frajka-Williams 2018) and the seasonal addition of the Greenland meltwater.

3) VERTICAL STRUCTURE AT THE SHELF BREAK

To understand how the difference in the off-shelf flux of meltwater arises when meltwater is either vertically distributed or concentrated at the surface, we compare the vertical profiles of the dye flux, EKE, and baroclinic conversion (T_2) across the UH8to2 experiments in Fig. 9.

The dye (Figs. 9a,d) fluxes have a structure, which is broadly consistent across both the northern and southern portions of the shelf. There is a surface maximum in off-shelf flux that is likely wind driven. Below the surface layer, the fluxes are uniformly decreasing with depth in the northern shelf region between 35 and 150 m. Along the southern portion of the shelf, there is a maximum in the off-shelf flux at 125-m depth. SPRD exhibits more off-shelf flux of dye compared to the SURF in both sections below the Ekman layer. Given that meltwater is only added to the upper 10 m of the water column in SURF, a considerable amount is fluxed off the shelf at depth, implying

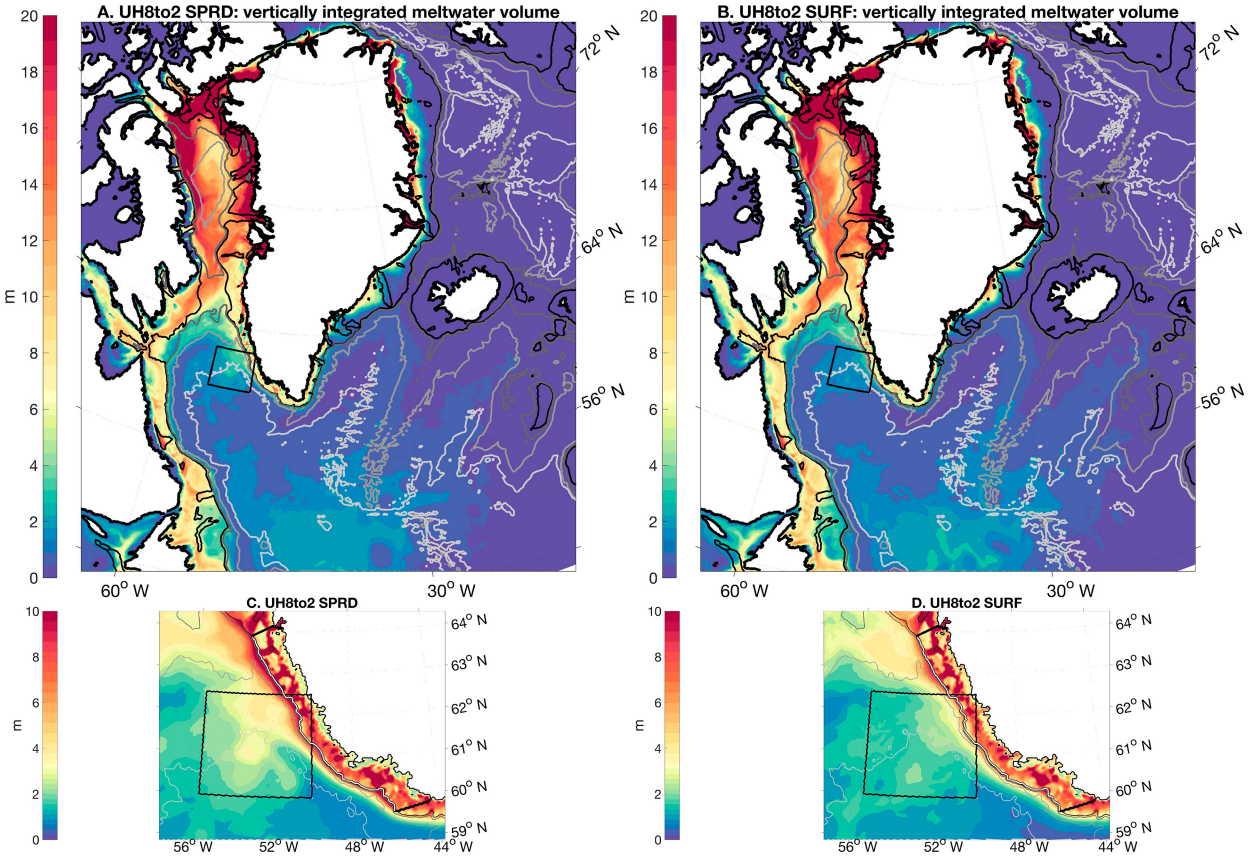

FIG. 7. Vertically integrated meltwater content (m) calculated from the monthly average dye concentration [Eq. (12)] in 1993–2012 for the (a) SPRD and (b) SURF. (c),(d) The meltwater content in the WGC eddy shedding region; note the difference in color scale from (a) to (b). The 200-, 800-, 2000-, and 3000-m isobaths are plotted from dark to light gray. The black box indicates the high EKE region as in Fig. 3.

that there is vertical mixing of meltwater on the shelf. Because the difference is at depth (below 35 m), we conclude that it is not related to changes in the wind-driven Ekman flux of the dye off the shelf and is likely driven by eddy processes. These differences must be considered in the context of the net convergence described in the previous section, as they are across a single section and are, therefore, not volume conserving.

The vertical structure of EKE at the shelf break shows the greatest EKE at the surface and a decrease with depth. The increase in the EKE in SPRD compared to SURF and CTRL is greatest along the northern shelf break (Fig. 9b). The change in the EKE is not uniform with depth, with the largest increase at the surface. There is a smaller change in the EKE with the addition of meltwater at the southern shelf break (Fig. 9e). To understand the source of this increase in the EKE, we compare the vertical profiles of T_2, which is the primary term converting mean to eddy energy at the shelf break.

The baroclinic conversion term T_2 has a maximum at depth (50–230 m) in both sections of the shelf (Figs. 9c,f). There is an additional very near-surface maximum in T_2 related to the density gradient at shallower depths. Along the northern shelf break (Fig. 9c), the maximum in baroclinic conversion at 165 m is 4.6×10^{-4} kg m^{-1} s^{-3} in SPRD, 2.5×10^{-4} kg m^{-1} s^{-3} in SURF, and 3.4×10^{-4} kg m^{-1} s^{-3} in CTRL. Along the southern shelf (Fig. 9f), the increase in the maximum of T_2 at depth is greatest in SPRD as well (8.0×10^{-4} kg m^{-1} s^{-3}), compared to SURF (5.6×10^{-4} kg m^{-1} s^{-3}) and CTRL (4.2×10^{-4} kg m^{-1} s^{-3}). In both regions, the increase in T_2 between CTRL and SURF is greater than the standard error of the mean, suggesting that this term can also be affected by meltwater added at the surface. The maximum of T_2 in the upper 10 m is greatest in SURF, indicating strong horizontal density gradients at the surface. This near-surface increase is why the vertically integrated change in T_2 was greater in SURF than SPRD over much of the shelf (Figs. 6a,b). Overall, there is an increase in baroclinic conversion at the shelf break when meltwater is vertically distributed.

We do not expect baroclinic conversion to directly cause off-shelf flux of meltwater; however, eddies do flux freshwater from the shelf into the basin (Castelao et al. 2019). The elevated EKE in SPRD and the increase in T_2 suggest that vertically distributed meltwater can increase eddy formation at the shelf break. The weak response in the vertical density flux (T_3, shown in the supplemental material) suggests that the increase in T_2 is linked to an increase in the horizontal density gradient at the shelf break. The horizontal density gradients

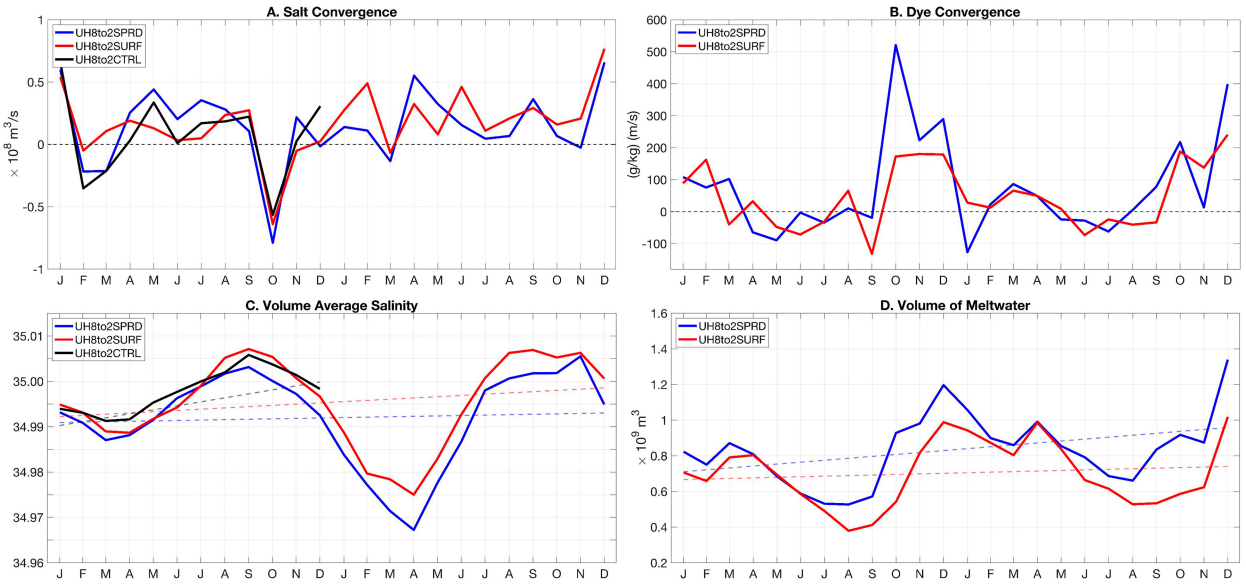

FIG. 8. Time series of (a) salt convergence (m s^{-1}), (b) dye convergence (g kg^{-1} m s^{-1}), (c) volume-averaged salinity, and (d) volume integrated meltwater (m^3), within the Labrador sea for SPRD (blue), SURF (red), and CTRL (black). For (c) and (d), the dashed lines show the linear trends in salt and meltwater volume, respectively. Only the meltwater volume trend in SPRD is significant based on an F test.

are the only parts of Eq. (6) (T_2), which are not in Eq. (7) (T_3) or the EKE, neither of which shows a robust change at depth. Furthermore, by adding meltwater, we are directly modifying the horizontal density gradients.

4. Discussion and conclusions

Using four coupled ocean/sea ice simulations, we investigated the impact of GIS meltwater on the West Greenland Current and the flux of salt into the Labrador Sea. We compare simulations without meltwater at two resolutions to highlight the need to represent mesoscale features. The comparison of CTRL01 and CTRL shows that there is an increase in the EKE and a narrower and faster WGC at higher resolution. Using the higher resolution (UH8to2) mesoscale eddy-resolving simulations, we compare the response to two GIS meltwater vertical distributions: at the surface, as is typically done, or vertically distributed, to represent mixing within fjords. We find that when meltwater is vertically distributed, the salinity in the eastern Labrador Sea decreases compared to cases with no meltwater (CTRL) or with meltwater concentrated in the surface layer (SURF). This suggests that the off-shelf flux of freshwater is sensitive to the vertical distribution of added meltwater.

For the mesoscale eddy-resolving configurations, we compare the energy budget terms in the meltwater forcing experiments to the control case with no meltwater. Including meltwater increases the speed of the coastal currents and decreases the salinity in the eastern Labrador Sea control volume. These impacts are summarized in Fig. 10. The increase in KEM is smaller in the case where melt is added to the surface only. There is an increase in the eddy potential energy on the shelf and extending into the Labrador Sea in both the meltwater forcing experiments. This increase in EPE is greater on the shelf in SURF compared to SPRD, but the increase in the basin relative to CTRL has a similar magnitude.

Using a control volume for the eastern Labrador Sea, we calculate the convergence of salt and volume average salinity. The change in the salt convergence is small with the addition of meltwater, but the average salinity within the control volume is lowest in SPRD. More meltwater is fluxed off the shelf in SPRD compared to SURF and the differences in meltwater export are greatest in the late fall and summer. The volume of meltwater within the Labrador Sea is greater in SPRD compared to SURF. Furthermore, in SPRD, there is a significant increasing trend in meltwater volume within the eastern Labrador Sea.

The eddy conversion terms from UH8to2 show that both baroclinic and barotropic instabilities contribute to the generation of eddies in this region. This result compares favorably with findings from other studies, despite differences in methodology. A study that using a model with resolution that is comparable to UH8to2 in the Labrador Sea, Rieck et al. (2019), similarly found contributions from both baroclinic and barotropic instabilities. Studies that used models, which can resolve similar dynamics to the CTRL01 ~ 1/10° grid, show that Irminger Rings are generated by baroclinic and barotropic instabilities in both idealized (Katsman et al. 2004) and realistic (Zhu et al. 2014) configurations. However, separate eddy-permitting simulations have shown that baroclinic instabilities primarily contribute to eddy generation (Luo et al. 2016; Saenko et al. 2014), while Eden and Böning (2002) concluded that barotropic instabilities are the dominant mechanism in eddy generation. The consistency of our findings with Rieck et al. (2019) and the inconsistency of the results from

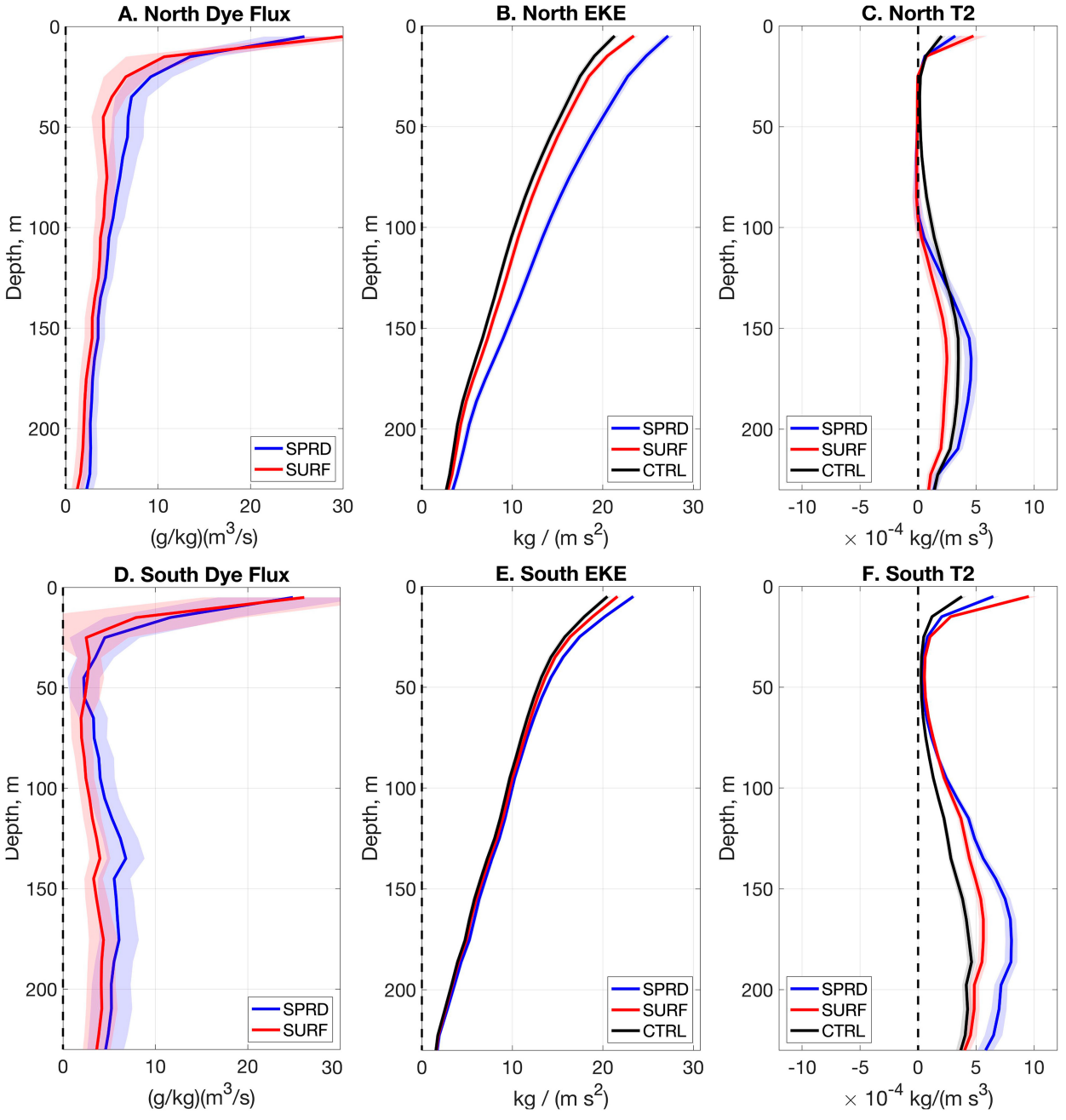

FIG. 9. Vertical profiles for the (a)–(c) northern shelf break and (d)–(f) southern shelf break averaged over 1992. Results from the three UH8to2 cases are shown. Vertical profiles plotted are (a),(d) net dye tracer flux (g kg^{-1} m^3 s^{-1}), (b),(e) average EKE (kg m^{-1} s^{-2}), and (c),(f) average T_2 (kg m^{-1} s^{-3}). Solid lines are the averages; for fluxes (a) and (d), the shaded areas are the standard-error-of-the-mean of the total flux time series; and for energy budget terms (b), (c), (e), and (f), the shaded areas are the standard-error-of-the-mean of the term along the shelf break.

eddy-permitting models indicate that a very high resolution is needed to determine the balance of baroclinic and barotropic conversion in this region. Beyond model resolution, the model setup, choice of eddy time scale, and portion of the water column, and shelf break to be considered all contribute to differences in energy conversion terms. Closing the energy budget off the West Greenland Current is beyond the scope of this study but would be needed to clarify these discrepancies.

The increase in the meltwater flux off the shelf is linked to an increase in baroclinic conversion at the shelf break. In the high-resolution simulations, baroclinic conversion is the primary mechanism of eddy formation on the shelf and at the shelf break, while barotropic conversion is the dominant term

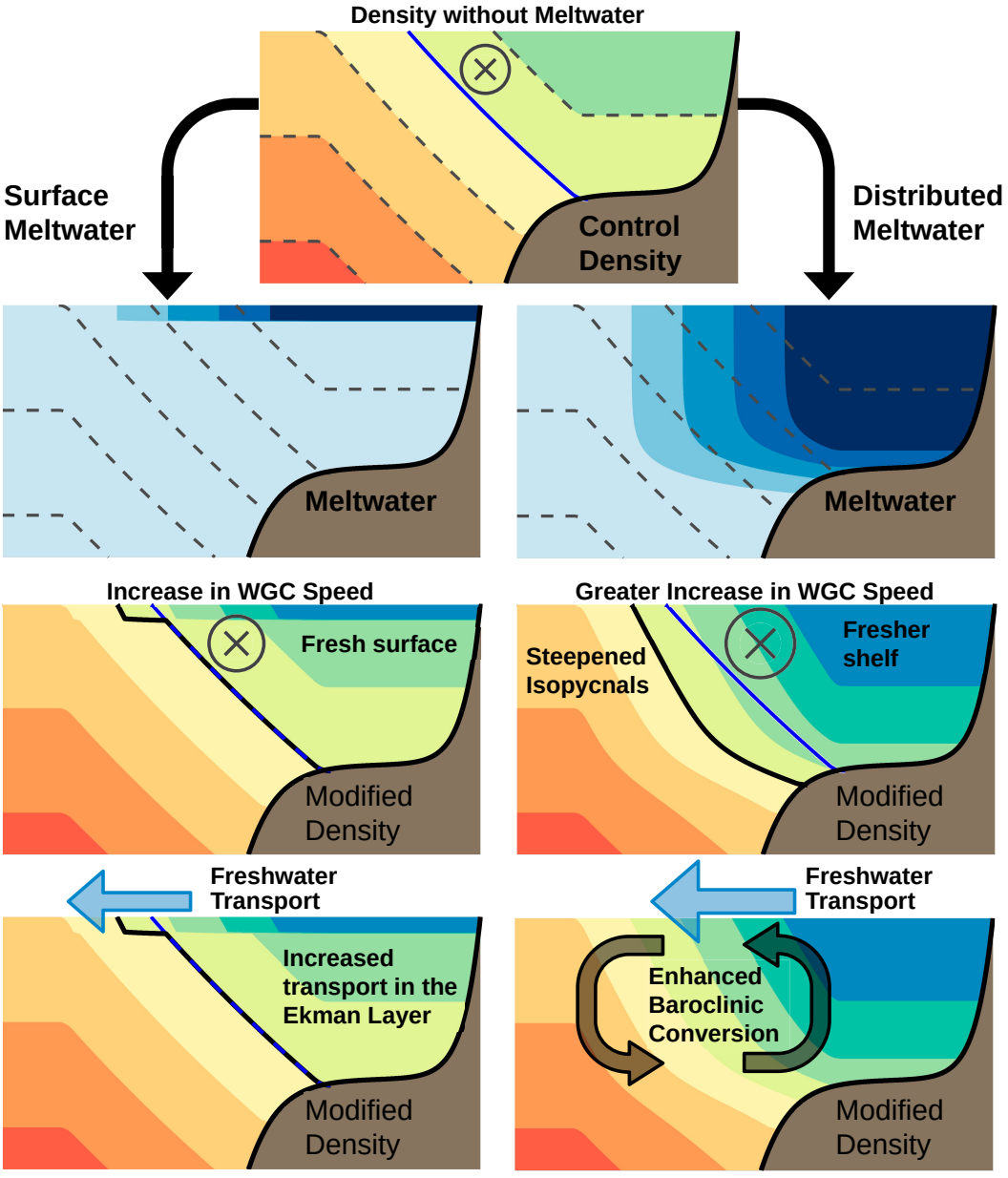

FIG. 10. Schematic representation of the response of density to the virtual salt flux perturbation. In the top row, the cross-shelf density gradient and slope current (representing the West Greenland Current) are shown. The second row shows the two meltwater perturbations, with the initial isopycnals shown in dashed lines. In the left column, the surface meltwater forcing freshens the surface and leads to a faster WGC. In the right column, the vertically distributed meltwater forcing steepens the isopycnals at the shelf break and the increase in the speed of the WGC is greater. The blue line is the original position of an isopycnal, and the black line is the same isopycnal after the meltwater forcing is applied. The bottom row shows the increased freshwater flux off the shelf in the Ekman layer in the surface case and the enhanced baroclinic conversion in the vertically distributed case.

in the basin. In SPRD, along the northern shelf break, baroclinic conversion is nearly twice what it is in SURF or CTRL. Vertically distributed meltwater increases the horizontal density gradients between 0 and 200 m, the depth range over which the meltwater perturbation is added, as illustrated in Fig. 10. As a result, there is an increase in the mean potential energy, which is converted to eddy potential energy through baroclinic conversion. These eddies could contribute to offshelf flux of dye below the Ekman layer. This proposed mechanism requires an ocean model that can resolve the formation of baroclinic instabilities. The one-tenth degree CTRL01 does not show the same formation of baroclinic instabilities at the

shelf break and, therefore, may not show the same sensitivity to the vertical distribution of meltwater (see the supplemental material for a map of T_2 in the CTRL01).

The increase in the EKE and surface current speed with the addition of GIS meltwater is consistent with studies that suggest that the ocean is accelerating in a changing climate (Hu et al. 2020; Peng et al. 2022; Martínez-Moreno et al. 2021). These studies have found this acceleration is "deep-reaching" (up to 2000 m) (Hu et al. 2020), in the upper 200 m (Peng et al. 2022), or identified in velocities derived from satellite altimetry (Martínez-Moreno et al. 2021). In these studies, the acceleration is not spatially uniform and possible acceleration of the deep ocean remains unresolved (Wunsch 2020). In the high-resolution simulations, we find that the increase in the speed is greater when the buoyancy forcing is distributed vertically rather than surface intensified.

There are several limitations inherent to the simulations used in this study that could be addressed in future work. All the simulations are uncoupled from the atmosphere and use a nonphysical virtual salt flux to represent meltwater fluxes, so there is no associated impact on the ocean heat or sea level. Further work is needed to determine whether the results of this study are robust when a true freshwater flux model is used. In addition, the comparison period for the control, surface meltwater, and vertically distributed meltwater cases is only 1 year, and there is only one realization of each configuration. During the year used for comparison, the NAO was in an extreme positive phase. Interannual variability could be examined in the high-resolution SPRD case, which has been run to the end of the CORE-II CIAF forcing cycle (2009). Newer atmospheric reanalysis is available such as JRA55 (Tsujino et al. 2018), as used by Fine et al. (2023), or ERA5 (Hersbach et al. 2020) and could be used in this model configuration. The products provide longer records with better spatial and temporal resolution than the CORE-II CIAF forcing (Large and Yeager 2009).

Despite such limitations, we find when using a mesoscale eddy-resolving ocean model, the impact of GIS meltwater on the West Greenland Current depends on how the meltwater is distributed vertically. When the mixing within fjords is represented by vertically distributing meltwater, there is a greater volume meltwater fluxed into the Labrador Sea, which has a lower average salinity. If GIS meltwater modifies shelf dynamics, resulting in increased flux of freshwater into the Labrador Sea, then the potential impact of meltwater on deep convection and AMOC variability could exceed the direct impacts expected based on the volume of meltwater alone. This points to the need for more sophisticated parameterizations of mixing within the fjords that link the GIS and the open ocean. These results were based on the period prior to the rapid increase in runoff that occurred in the mid-1990s (Bamber et al. 2018). Examining the trends and multiyear variability of meltwater flux into the Labrador Sea is further work that can be done with the vertically distributed meltwater configuration.

Acknowledgments. T. J. Morrison, J. L. McClean, S. T. Gille, and D. P. Ivanova were funded by the DOE Office of Science Grants: DE-SC0014440 and DE-SC0020073. This research used the resources of the National Energy Research Scientific Computing Center (NERSC), a U.S. Department of Energy Office of Science User Facility located at Lawrence Berkeley National Laboratory, operated under Contract DE-AC02-05CH11231 using NERSC Awards: BER-ERCAP (01729, 04299, 10177, 13967, 17512, 20372, 23627) and ALCC-ERCAP (16316, 19007). We thank Elizabeth Hunke (LANL) for contributing to the CICE5 parameter choices, and John Ritchie and Judy Gaukel for their contributions to configuring the UH8to2 bathymetry. Thanks to S. Griffies and M. Harrison at the Geophysical Fluid Dynamics Laboratory for their helpful feedback on the manuscript. We also thank two anonymous reviewers for their helpful feedback.

Data availability statement. The metrics calculated for this work are available on a subset of the model grid. These data are hosted by the University of California, San Diego, library at https://doi.org/10.6075/J07H1JS3.

REFERENCES

Bamber, J. L., A. J. Tedstone, M. D. King, I. M. Howat, E. M. Enderlin, M. R. van den Broeke, and B. Noel, 2018: Land ice freshwater budget of the Arctic and North Atlantic Oceans: 1. Data, methods, and results. *J. Geophys. Res. Oceans*, **123**, 1827–1837, https://doi.org/10.1002/2017JC013605.

Beaird, N., F. Straneo, and W. Jenkins, 2015: Spreading of Greenland meltwaters in the ocean revealed by noble gases. *Geophys. Res. Lett.*, **42**, 7705–7713, https://doi.org/10.1002/2015GL065003.

——, ——, and ——, 2017: Characteristics of meltwater export from Jakobshavn Isbræ and Ilulissat Icefjord. *Ann. Glaciol.*, **58**, 107–117, https://doi.org/10.1017/aog.2017.19.

Beaird, N. L., F. Straneo, and W. Jenkins, 2018: Export of strongly diluted Greenland meltwater from a major glacial fjord. *Geophys. Res. Lett.*, **45**, 4163–4170, https://doi.org/10.1029/2018GL077000.

Beckmann, A., C. W. Böning, B. Brügge, and D. Stammer, 1994: On the generation and role of eddy variability in the central North Atlantic Ocean. *J. Geophys. Res.*, **99**, 20 381–20 391, https://doi.org/10.1029/94JC01654.

Böning, C. W., and R. G. Budich, 1992: Eddy dynamics in a primitive equation model: Sensitivity to horizontal resolution and friction. *J. Phys. Oceanogr.*, **22**, 361–381, https://doi.org/10.1175/1520-0485(1992)022<0361:EDIAPE>2.0.CO;2.

——, E. Behrens, A. Biastoch, K. Getzlaff, and J. L. Bamber, 2016: Emerging impact of Greenland meltwater on deepwater formation in the North Atlantic Ocean. *Nat. Geosci.*, **9**, 523–527, https://doi.org/10.1038/ngeo2740.

Bracco, A., J. Pedlosky, and R. S. Pickart, 2008: Eddy formation near the west coast of Greenland. *J. Phys. Oceanogr.*, **38**, 1992–2002, https://doi.org/10.1175/2008JPO3669.1.

Brandt, P., F. A. Schott, A. Funk, and C. S. Martins, 2004: Seasonal to interannual variability of the eddy field in the Labrador Sea from satellite altimetry. *J. Geophys. Res.*, **109**, C02028, https://doi.org/10.1029/2002JC001551.

Carroll, D., and Coauthors, 2016: The impact of glacier geometry on meltwater plume structure and submarine melt in Greenland fjords. *Geophys. Res. Lett.*, **43**, 9739–9748, https://doi.org/10.1002/2016GL070170.

Castelao, R. M., and Coauthors, 2019: Controls on the transport of meltwater from the southern Greenland ice sheet in the Labrador Sea. *J. Geophys. Res. Oceans*, **124**, 3551–3560, https://doi.org/10.1029/2019JC015159.

Chafik, L., and T. Rossby, 2019: Volume, heat, and freshwater divergences in the subpolar North Atlantic suggest the Nordic Seas as key to the state of the meridional overturning circulation. *Geophys. Res. Lett.*, **46**, 4799–4808, https://doi.org/10.1029/2019GL082110.

Chanut, J., B. Barnier, W. Large, L. Debreu, T. Penduff, J. M. Molines, and P. Mathiot, 2008: Mesoscale eddies in the Labrador Sea and their contribution to convection and restratification. *J. Phys. Oceanogr.*, **38**, 1617–1643, https://doi.org/10.1175/2008JPO3485.1.

Dai, A., and K. E. Trenberth, 2002: Estimates of freshwater discharge from continents: Latitudinal and seasonal variations. *J. Hydrometeor.*, **3**, 660–687, https://doi.org/10.1175/1525-7541(2002)003<0660:EOFDFC>2.0.CO;2.

de Jong, M. F., A. S. Bower, and H. H. Furey, 2014: Two years of observations of warm-core anticyclones in the Labrador Sea and their seasonal cycle in heat and salt stratification. *J. Phys. Oceanogr.*, **44**, 427–444, https://doi.org/10.1175/JPO-D-13-070.1.

Desbruyères, D. G., H. Mercier, G. Maze, and N. Daniault, 2019: Surface predictor of overturning circulation and heat content change in the subpolar North Atlantic. *Ocean Sci.*, **15**, 809–817, https://doi.org/10.5194/os-15-809-2019.

Dukhovskoy, D. S., and Coauthors, 2016: Greenland freshwater pathways in the sub-Arctic seas from model experiments with passive tracers. *J. Geophys. Res. Oceans*, **121**, 877–907, https://doi.org/10.1002/2015JC011290.

Dukowicz, J. K., and R. D. Smith, 1994: Implicit free-surface method for the Bryan-Cox-Semtner ocean model. *J. Geophys. Res.*, **99**, 7991–8014, https://doi.org/10.1029/93JC03455.

Eden, C., 2007: Eddy length scales in the North Atlantic Ocean. *J. Geophys. Res.*, **112**, C06004, https://doi.org/10.1029/2006JC003901.

——, and C. Böning, 2002: Sources of eddy kinetic energy in the Labrador Sea. *J. Phys. Oceanogr.*, **32**, 3346–3363, https://doi.org/10.1175/1520-0485(2002)032<3346:SOEKEI>2.0.CO;2.

Fine, E. C., J. L. McClean, D. P. Ivanova, A. P. Craig, A. J. Wallcraft, E. P. Chassignet, and E. C. Hunke, 2023: Arctic ice-ocean interactions in an 8-to-2 kilometer resolution global model. *Ocean Modell.*, **184**, 102228, https://doi.org/10.1016/j.ocemod.2023.102228.

Foukal, N. P., R. Gelderloos, and R. S. Pickart, 2020: A continuous pathway for fresh water along the East Greenland Shelf. *Sci. Adv.*, **6**, eabc4254, https://doi.org/10.1126/sciadv.abc4254.

Funk, A., P. Brandt, and T. Fischer, 2009: Eddy diffusivities estimated from observations in the Labrador Sea. *J. Geophys. Res.*, **114**, C04001, https://doi.org/10.1029/2008JC005098.

Gent, P. R., and J. C. Mcwilliams, 1990: Isopycnal mixing in ocean circulation models. *J. Phys. Oceanogr.*, **20**, 150–155, https://doi.org/10.1175/1520-0485(1990)020<0150:IMIOCM>2.0.CO;2.

Gillard, L. C., X. Hu, P. G. Myers, and J. L. Bamber, 2016: Meltwater pathways from marine terminating glaciers of the Greenland ice sheet. *Geophys. Res. Lett.*, **43**, 10 873–10 882, https://doi.org/10.1002/2016GL070969.

Gou, R., C. Feucher, C. Pennelly, and P. G. Myers, 2021: Seasonal cycle of the coastal West Greenland current system between Cape Farewell and Cape Desolation from a very high-resolution numerical model. *J. Geophys. Res. Oceans*, **126**, e2020JC017017, https://doi.org/10.1029/2020JC017017.

Hallberg, R., 2013: Using a resolution function to regulate parameterizations of oceanic mesoscale eddy effects. *Ocean Modell.*, **72**, 92–103, https://doi.org/10.1016/j.ocemod.2013.08.007.

Håvik, L., K. Våge, R. S. Pickart, B. Harden, W.-J. Appen, S. Jónsson, and S. Østerhus, 2017: Structure and variability of the Shelfbreak East Greenland current north of Denmark Strait. *J. Phys. Oceanogr.*, **47**, 2631–2646, https://doi.org/10.1175/JPO-D-17-0062.1.

Hecht, M., and Coauthors, 2019: E3SMv0-HiLAT: A modified climate system model targeted for the study of high-latitude processes. *J. Adv. Model. Earth Syst.*, **11**, 2814–2843, https://doi.org/10.1029/2018MS001524.

Hersbach, H., and Coauthors, 2020: The ERA5 global reanalysis. *Quart. J. Roy. Meteor. Soc.*, **146**, 1999–2049, https://doi.org/10.1002/qj.3803.

Holliday, N. P., S. Bacon, S. A. Cunningham, S. F. Gary, J. Karstensen, B. A. King, F. Li, and E. L. McDonagh, 2018: Subpolar North Atlantic overturning and gyre-scale circulation in the summers of 2014 and 2016. *J. Geophys. Res. Oceans*, **123**, 4538–4559, https://doi.org/10.1029/2018JC013841.

Hu, S., J. Sprintall, C. Guan, M. J. McPhaden, F. Wang, D. Hu, and W. Cai, 2020: Deep-reaching acceleration of global mean ocean circulation over the past two decades. *Sci. Adv.*, **6**, eaax7727, https://doi.org/10.1126/sciadv.aax7727.

Hunke, E. C., W. H. Lipscomb, A. K. Turner, N. Jeffery, and S. Elliott, 2010: CICE: The Los Alamos Sea Ice Model documentation and software user's manual, version 4.1. Doc. LA-CC-06-012, 76 pp., https://csdms.colorado.edu/w/images/CICE_documentation_and_software_user's_manual.pdf.

Hurrell, J. W., and Coauthors, 2013: The Community Earth System Model: A framework for collaborative research. *Bull. Amer. Meteor. Soc.*, **94**, 1339–1360, https://doi.org/10.1175/BAMS-D-12-00121.1.

Katsman, C. A., M. A. Spall, and R. S. Pickart, 2004: Boundary current eddies and their role in the restratification of the Labrador Sea. *J. Phys. Oceanogr.*, **34**, 1967–1983, https://doi.org/10.1175/1520-0485(2004)034<1967:BCEATR>2.0.CO;2.

Large, W. G., and S. G. Yeager, 2009: The global climatology of an interannually varying air–sea flux data set. *Climate Dyn.*, **33**, 341–364, https://doi.org/10.1007/s00382-008-0441-3.

Laurindo, L. C., A. J. Mariano, and R. Lumpkin, 2017: An improved near-surface velocity climatology for the global ocean from drifter observations. *Deep-Sea Res. I*, **124**, 73–92, https://doi.org/10.1016/j.dsr.2017.04.009.

Lilly, J. M., P. B. Rhines, F. Schott, K. Lavender, J. Lazier, U. Send, and E. D'Asaro, 2003: Observations of the Labrador Sea eddy field. *Prog. Oceanogr.*, **59**, 75–176, https://doi.org/10.1016/j.pocean.2003.08.013.

Lozier, M. S., and Coauthors, 2019: A sea change in our view of overturning in the subpolar North Atlantic. *Science*, **363**, 516–521, https://doi.org/10.1126/science.aau6592.

Luo, H., R. M. Castelao, A. K. Rennermalm, M. Tedesco, A. Bracco, P. L. Yager, and T. L. Mote, 2016: Oceanic transport of surface meltwater from the southern Greenland Ice Sheet. *Nat. Geosci.*, **9**, 528–532, https://doi.org/10.1038/ngeo2708.

Majumder, S., R. M. Castelao, and C. M. Amos, 2021: Freshwater variability and transport in the Labrador Sea from in situ and satellite observations. *J. Geophys. Res. Oceans*, **126**, e2020JC016751, https://doi.org/10.1029/2020JC016751.

Mana, P. P., and L. Zanna, 2014: Toward a stochastic parameterization of ocean mesoscale eddies. *Ocean Modell.*, **79**, 1–20, https://doi.org/10.1016/j.ocemod.2014.04.002.

Marshall, J., and F. Schott, 1999: Open-ocean convection: Observations, theory, and models. *Rev. Geophys.*, **37** (1), 1–64, https://doi.org/10.1029/98RG02739.

Martínez-Moreno, J., A. M. Hogg, M. H. England, N. C. Constantinou, A. E. Kiss, and A. K. Morrison, 2021: Global changes in oceanic mesoscale currents over the satellite altimetry record. *Nat. Climate Change*, **11**, 397–403, https://doi.org/10.1038/s41558-021-01006-9.

Moon, T., D. A. Sutherland, D. Carroll, D. Felikson, L. Kehrl, and F. Straneo, 2018: Subsurface iceberg melt key to Greenland fjord freshwater budget. *Nat. Geosci.*, **11**, 49–54, https://doi.org/10.1038/s41561-017-0018-z.

Morlighem, M., and Coauthors, 2017: BedMachine v3: Complete bed topography and ocean bathymetry mapping of Greenland from multibeam echo sounding combined with mass conservation. *Geophys. Res. Lett.*, **44**, 11 051–11 061, https://doi.org/10.1002/2017GL074954.

Noël, B., and Coauthors, 2018: Modelling the climate and surface mass balance of polar ice sheets using RACMO2–Part 1: Greenland (1958–2016). *Cryosphere*, **12**, 811–831, https://doi.org/10.5194/tc-12-811-2018.

Pacini, A., and R. S. Pickart, 2022: Meanders of the West Greenland current near Cape Farewell. *Deep-Sea Res. I*, **179**, 103664, https://doi.org/10.1016/j.dsr.2021.103664.

——, and Coauthors, 2020: Mean conditions and seasonality of the West Greenland boundary current system near Cape Farewell. *J. Phys. Oceanogr.*, **50**, 2849–2871, https://doi.org/10.1175/JPO-D-20-0086.1.

Peng, Q., S.-P. Xie, D. Wang, R. X. Huang, G. Chen, Y. Shu, J.-R. Shi, and W. Liu, 2022: Surface warming–induced global acceleration of upper ocean currents. *Sci. Adv.*, **8**, eabj8394, https://doi.org/10.1126/sciadv.abj8394.

Pennelly, C., X. Hu, and P. G. Myers, 2019: Cross-isobath freshwater exchange within the North Atlantic subpolar gyre. *J. Geophys. Res. Oceans*, **124**, 6831–6853, https://doi.org/10.1029/2019JC015144.

Petit, T., M. S. Lozier, S. A. Josey, and S. A. Cunningham, 2020: Atlantic deep water formation occurs primarily in the Iceland Basin and Irminger Sea by local buoyancy forcing. *Geophys. Res. Lett.*, **47**, e2020GL091028, https://doi.org/10.1029/2020GL091028.

Pickart, R. S., D. J. Torres, and R. A. Clarke, 2002: Hydrography of the Labrador Sea during active convection. *J. Phys. Oceanogr.*, **32**, 428–457, https://doi.org/10.1175/1520-0485(2002)032<0428:HOTLSD>2.0.CO;2.

Rieck, J. K., C. W. Böning, and K. Getzlaff, 2019: The nature of eddy kinetic energy in the Labrador Sea: Different types of mesoscale eddies, their temporal variability, and impact on deep convection. *J. Phys. Oceanogr.*, **49**, 2075–2094, https://doi.org/10.1175/JPO-D-18-0243.1.

Roberts, M. J., and Coauthors, 2020: Sensitivity of the Atlantic meridional overturning circulation to model resolution in CMIP6 HighResMIP simulations and implications for future changes. *J. Adv. Model. Earth Syst.*, **12**, e2019MS002014, https://doi.org/10.1029/2019MS002014.

Rossby, T., C. Flagg, L. Chafik, B. Harden, and H. Søiland, 2018: A direct estimate of volume, heat, and freshwater exchange across the Greenland-Iceland-Faroe-Scotland Ridge. *J. Geophys. Res. Oceans*, **123**, 7139–7153, https://doi.org/10.1029/2018JC014250.

Saenko, O. A., F. Dupont, D. Yang, P. G. Myers, I. Yashayaev, and G. C. Smith, 2014: Role of resolved and parameterized eddies in the Labrador Sea balance of heat and buoyancy. *J. Phys. Oceanogr.*, **44**, 3008–3032, https://doi.org/10.1175/JPO-D-14-0041.1.

Schauer, U., and M. Losch, 2019: "Freshwater" in the ocean is not a useful parameter in climate research. *J. Phys. Oceanogr.*, **49**, 2309–2321, https://doi.org/10.1175/JPO-D-19-0102.1.

Schulze Chretien, L. M., and E. Frajka-Williams, 2018: Wind-driven transport of fresh shelf water into the upper 30 m of the Labrador Sea. *Ocean Sci.*, **14**, 1247–1264, https://doi.org/10.5194/os-14-1247-2018.

Steele, M., R. Morley, and W. Ermold, 2001: PHC: A global ocean hydrography with a high-quality Arctic Ocean. *J. Climate*, **14**, 2079–2087, https://doi.org/10.1175/1520-0442(2001)014<2079:PAGOHW>2.0.CO;2.

Stewart, A. L., A. Klocker, and D. Menemenlis, 2019: Acceleration and overturning of the Antarctic slope current by winds, eddies, and tides. *J. Phys. Oceanogr.*, **49**, 2043–2074, https://doi.org/10.1175/JPO-D-18-0221.1.

Straneo, F., and C. Cenedese, 2015: The dynamics of Greenland's glacial fjords and their role in climate. *Annu. Rev. Mar. Sci.*, **7**, 89–112, https://doi.org/10.1146/annurev-marine-010213-135133.

Sutherland, D. A., and R. S. Pickart, 2008: The East Greenland coastal current: Structure, variability, and forcing. *Prog. Oceanogr.*, **78**, 58–77, https://doi.org/10.1016/j.pocean.2007.09.006.

Trodahl, M., and P. E. Isachsen, 2018: Topographic influence on baroclinic instability and the mesoscale eddy field in the northern North Atlantic Ocean and the Nordic Seas. *J. Phys. Oceanogr.*, **48**, 2593–2607, https://doi.org/10.1175/JPO-D-17-0220.1.

Tsujino, H., and Coauthors, 2018: JRA-55 based surface dataset for driving ocean–sea-ice models (JRA55-do). *Ocean Modell.*, **130**, 79–139, https://doi.org/10.1016/j.ocemod.2018.07.002.

Weatherall, P., and Coauthors, 2015: A new digital bathymetric model of the world's oceans. *Earth Space Sci.*, **2**, 331–345, https://doi.org/10.1002/2015EA000107.

Weijer, W., and Coauthors, 2019: Stability of the Atlantic meridional overturning circulation: A review and synthesis. *J. Geophys. Res. Oceans*, **124**, 5336–5375, https://doi.org/10.1029/2019JC015083.

Wunsch, C., 2020: Is the ocean speeding up? Ocean surface energy trends. *J. Phys. Oceanogr.*, **50**, 3205–3217, https://doi.org/10.1175/JPO-D-20-0082.1.

Yeager, S., and Coauthors, 2021: An outsized role for the Labrador Sea in the multidecadal variability of the Atlantic overturning circulation. *Sci. Adv.*, **7**, eabh3592, https://doi.org/10.1126/sciadv.abh3592.

Yin, J., R. J. Stouffer, M. J. Spelman, and S. M. Griffies, 2010: Evaluating the uncertainty induced by the virtual salt flux assumption in climate simulations and future projections. *J. Climate*, **23**, 80–96, https://doi.org/10.1175/2009JCLI3084.1.

Yu, L., Y. Gao, and O. H. Otterå, 2016: The sensitivity of the Atlantic meridional overturning circulation to enhanced freshwater discharge along the entire, eastern and western coast of Greenland. *Climate Dyn.*, **46**, 1351–1369, https://doi.org/10.1007/s00382-015-2651-9.

Zhu, J., E. Demirov, Y. Zhang, and A. Polomska-Harlick, 2014: Model simulations of mesoscale eddies and deep convection in the Labrador Sea. *Adv. Atmos. Sci.*, **31**, 743–754, https://doi.org/10.1007/s00376-013-3107-y.